



# Cloud Algorithm Development Support Study Final Report

DISTRIBUTION : Thierry MARBACH (EUMETSAT)  
Bertrand FOUGNIE (EUMETSAT)  
Jérôme RIEDI (LOA / ICARE)  
Didier RAMON (HYGEOS)

INFORMATION : A study performed by University of Lille with support from HYGEOS-Earth Observation

REPORT EDITOR : J. RIEDI VISA :

REF. : LOA/3MI-CLD-ADSS/JR

INITIAL REPORT DELIVERY: 4<sup>th</sup> Decembre 2019

LAST UPDATED: 6<sup>th</sup> Decembre 2019

## Revision history

- Revision 01 : 6<sup>th</sup> December 2019 – initial delivery

1	INTRODUCTION .....	5
2	THEORETICAL BASIS FOR CLOUD PROPERTIES RETRIEVAL FROM 3MI .....	6
2.1	<b>Brief overview of initial 3MI Day-1 algorithm proposal .....</b>	<b>6</b>
2.2	<b>Description of Day-1 cloud properties retrieval algorithms .....</b>	<b>7</b>
2.2.1	Summary of implemented Day-1 cloud properties retrieval algorithms .....	7
2.2.2	Theoretical basis and heritage for Day-1 cloud properties retrieval algorithms.....	7
3	DESCRIPTION OF THE 3MI-CLD-L2 PROCESSING SOFTWARE .....	12
3.1	<b>Prototype software main functions and logical workflow .....</b>	<b>12</b>
3.2	<b>Current status of algorithm implementation .....</b>	<b>15</b>
3.2.1	List of implemented products .....	15
3.2.2	Evaluation of NRT compatibility .....	16
4	ASSESSMENT OF RETRIEVED PROPERTIES.....	18
4.1	<b>General approach.....</b>	<b>18</b>
4.2	<b>Specifics for comparison of retrievals against V3.2 and V4.1 input parameters.....</b>	<b>19</b>
5	RESULTS FOR V3 TEST DATA.....	21
5.1	<b>Cloud Detection.....</b>	<b>21</b>
5.2	<b>Cloud Thermodynamic Phase .....</b>	<b>22</b>
5.3	<b>Cloud Top Pressure from Rayleigh signal and O2-A band Scene Apparent Pressure .....</b>	<b>23</b>
5.3.1	Examples.....	23
5.4	<b>Cloud Top Pressure from O2-A band.....</b>	<b>24</b>
5.4.1	Global Comparison .....	24
5.4.2	Comparison by cloud phase.....	25
5.4.3	Cloud Apparent pressure & Cloud Middle Pressure from O2-A band .....	26
5.5	<b>Cloud Geometrical Thickness.....</b>	<b>27</b>
5.6	<b>Multilayered Clouds Occurrence .....</b>	<b>28</b>
5.7	<b>Cloud Optical Thickness.....</b>	<b>29</b>
5.7.1	Global Comparison .....	29
5.7.2	Comparison by cloud phase.....	30
5.8	<b>Cloud Particle Effective Radius .....</b>	<b>31</b>
5.8.1	Global Comparison .....	31
5.8.2	Comparison by cloud phase .....	32
5.9	<b>Cloud Spherical Albedo &amp; Shortwave Albedo .....</b>	<b>33</b>
5.9.1	Examples.....	33
6	RESULTS FOR V4 TEST DATA.....	34

<b>6.1</b>	<b>Cloud Detection.....</b>	<b>34</b>
<b>6.2</b>	<b>Cloud Thermodynamic Phase .....</b>	<b>35</b>
<b>6.3</b>	<b>Cloud Top Pressure from Rayleigh signal and O2-A band Scene Apparent Pressure .....</b>	<b>36</b>
6.3.1	Examples.....	36
<b>6.4</b>	<b>Cloud Top Pressure from O2-A band.....</b>	<b>37</b>
6.4.1	Global Comparison .....	37
6.4.2	Comparison by cloud phase .....	38
6.4.3	Cloud Apparent pressure & Cloud Middle Pressure from O2-A band .....	39
<b>6.5</b>	<b>Cloud Geometrical Thickness.....</b>	<b>40</b>
<b>6.6</b>	<b>Multilayered Clouds Occurrence .....</b>	<b>41</b>
<b>6.7</b>	<b>Cloud Optical Thickness.....</b>	<b>42</b>
6.7.1	Global Comparison .....	42
6.7.2	Comparison by cloud phase .....	43
<b>6.8</b>	<b>Cloud Particle Effective Radius .....</b>	<b>44</b>
6.8.1	Global Comparison .....	44
6.8.2	Comparison by cloud phase .....	45
<b>6.9</b>	<b>Cloud Spherical Albedo &amp; Shortwave Albedo .....</b>	<b>46</b>
6.9.1	Examples.....	46
<b>7</b>	<b>DISCUSSION OF RESULTS AND ACCURACY EVALUATION .....</b>	<b>47</b>
<b>7.1</b>	<b>Expression of requirements.....</b>	<b>47</b>
<b>7.2</b>	<b>Results discussion.....</b>	<b>49</b>
7.2.1	Cloud Detection.....	49
7.2.2	Cloud Thermodynamic Phase.....	49
7.2.3	Cloud Top Pressure from Rayleigh (PRAY) and Scene Apparent Pressure (PAPP).....	50
7.2.4	Cloud Top Pressure from O2-A band (CTOP).....	50
7.2.5	Cloud Apparent pressure & Cloud Middle Pressure from O2-A band .....	51
7.2.6	Cloud Geometrical Thickness .....	51
7.2.7	Multilayered Clouds Occurrence.....	52
7.2.8	Cloud Optical Thickness .....	52
7.2.9	Cloud Particle Effective Radius.....	53
7.2.10	Cloud Spherical Albedo & Shortwave Albedo.....	53
<b>8</b>	<b>CONCLUSIONS AND PERSPECTIVES.....</b>	<b>53</b>
<b>8.1</b>	<b>Conclusions .....</b>	<b>53</b>
<b>8.2</b>	<b>Expected potential improvements.....</b>	<b>54</b>
8.2.1	Cloud effective radius from polarization .....	54
8.2.2	Uncertainties estimates.....	54
8.2.3	Cloud ShortWave albedo .....	54
8.2.4	Vertical variability of cloud properties .....	54
<b>9</b>	<b>REFERENCES .....</b>	<b>57</b>

10 LIST OF FIGURES.....60

## 1 Introduction

This document reports on the study performed to support the algorithm development for retrieval of cloud properties from the Multichannel, Multiviewing, Multipolarisation Instrument (3MI).

In **section 2**, an **overview of theoretical basis** for cloud properties retrieval is provided based on literature and readily existing algorithms that have been developed for processing of POLDER and MODIS observations, either in standalone configuration or through the synergy of both sensors.

Then a **description of a prototype software** developed for processing of 3MI L1C data is provided in **Section 3**, focusing on its main characteristics including details of main processing steps and description of implemented science modules.

The performances of retrieval algorithms are evaluated through processing of 3MI science test datasets and comparison between retrieved quantities to their input counterparts used for generation of the test datasets.

In **section 4**, we present the **methodology** adopted for the products evaluation by comparison to relevant parameters used as input to the simulation software.

**Example products** are illustrated and **comparison results** are presented in **sections 5 and 6** respectively for the products derived from processing of L1C test data set (TDS) V3.2 and 4.1. TDS V3.2 corresponds to simulations performed using simplified description of atmospheric conditions particularly single phase homogeneous single cloud layers with no aerosol mixing in cloudy skies, while aerosols are also described using a single model and profile for any given pixel. At the opposite, TDS V4.1 have been simulated using much more complex assumptions about atmospheric properties and vertical structure. Of particular interest to the present study, clouds are described as extended non-homogeneous layers of various geometrical extent, they can contain both liquid and ice phase for any given layer and aerosols are also distributed vertically through the atmospheric column. Furthermore, the extinction profiles for cloud layers are highly variable and follow the distribution obtained from ECMWF reanalysis for the simulated day.

A discussion of **algorithm performances** is provided in **section 7**, summarizing the achieved accuracy whenever possible and comparing those to mission requirements. **Conclusions and perspectives** for future development are provided in the last **section 8**.

## 2 Theoretical basis for cloud properties retrieval from 3MI

### 2.1 Brief overview of initial 3MI Day-1 algorithm proposal

A review of the initially proposed 3MI Day-1 algorithms has been performed at the beginning of the present study. Most proposed algorithms did not take full advantage of the 3MI capabilities or relying on controversial theoretical basis. Among most noticeable points identified from the review we noted the following for the proposed cloud products:

**Cloud Mask (3MI standalone):** the proposed approach used thresholds-based test but did not take advantage of the directional information except for the detection of rainbow. Moreover, there was no clear logic for combining the several tests proposed and no confidence or Quality Assessment flag were provided.

**Cloud Phase:** Initial algorithm used polarization and SWIR/VNIR ratios but logic for decision was not defined. This was critically missing since algorithm must be able to handle varying geometries sampled by 3MI.

**Cloud Optical Thickness, Cloud Effective Radius and LWP:** proposed algorithm used a bispectral technique (Nakajima & King, 1990) applied to 410 nm and 1650 nm or 2130 nm channels. Although the approach has a long history of application on AVHRR and MODIS, the implementation choices were highly questionable on several aspect : (1) implementation used asymptotic regime theory only limiting retrievals to thick clouds only, (2) the choice of the 410 nm channel was controversial due to significant contribution of Rayleigh scattering at this wavelength and the uncertainty introduced by cloud altitude and geometrical extent due to cloud/atmosphere couplin, (3) ice crystal models were not state of the art. (4) LUT were too coarse to adequately represent features of liquid clouds angular signatures (BRDF), (5) logic for CER/COT selection needed consolidation.

**Cloud Effective Radius from polarization:** initial algorithm used angular polarization at 1650nm instead of original 865nm but logic was not clearly described. Also, no use of polarization multispectral information was made even though it is required to attempt retrieval at full resolution. The proposed approach was directly adapted from Bréon and Goloub (1999) which is not applicable to full 3MI resolution. Finally, a fixed variance was assumed for the size distribution whereas it is well established that this parameter strongly impacts signal outside of primary rainbow.

**Cloud Top Height (from O2-A band):** a semi-analytical approach was proposed based on Look-Up Tables. The proposed analytical formulation could be better in principle than the original POLDER algorithm. However, the formulation didn't account for cloud geometrical thickness variability when algorithms developed for POLDER (Ferlay et al, 2016) and those currently being developed for VII or proposed for 3MI provided numerous evidences that cloud geometrical thickness and vertical extinction profile have a strong impact on O2-A band signal. Finally, no use of Rayleigh scattering signal was foreseen: use of polarized multispectral information had been dropped to the benefit of O2-A band only retrieval. Doing so clearly prevented to obtain useful information for detection of aerosol above cloud or multilayer situation.

Following this initial review, it was decided to focus on implementing a different set of algorithms derived from the operational POLDER processing software in order to benefit from the strong POLDER heritage. Additionally, enhanced algorithms using synergy of POLDER and MODIS observations were recommended to benefit fully from the 3MI extended spectral range. The following section provides the theoretical basis for those algorithms.

## 2.2 Description of Day-1 cloud properties retrieval algorithms

### 2.2.1 Summary of implemented Day-1 cloud properties retrieval algorithms

The following cloud products retrievals have been implemented in the delivered prototype software (Table 1). Many of those algorithms are direct heritage from the Cloud, Water Vapor and Earth Radiation Budget suite of products developed for processing of the POLDER observations. Thanks to the 3MI extended spectral range (SWIR channels), the Cloud Mask and Cloud Phase algorithm have inherited some of the capabilities implemented within the POLDER/MODIS joint cloud/aerosol retrieval software (Riedi et al, 2010) and similarly we implemented the bispectral technique (Nakajima & King, 1990) that has been used extensively to infer cloud particle size from several atmosphere observing missions (Platnick et al, 2016).

Product	Retrieval method	Heritage	Multiangle
Cloud mask	Test ensemble	POLDER/MODIS	no
Cloud Phase	Decision tree & LUT	POLDER/MODIS	no
Multilayer flag	Decision tree	POLDER	no
Cloud Optical thickness	LUT	POLDER	yes
Effective size from bispectral (ice and liquid)	LUT	MODIS	yes
Droplet effective radius (liquid only) from polarisation	Optimal estimation	POLDER	no
Rayleigh cloud top pressure	Semi-analytical	POLDER	yes
O2-A band cloud pressure	Semi-analytical	POLDER	yes
Cloud vertical altitude & extent	Statistical parametrization	POLDER	no
Cloud spectral albedo	LUT	POLDER	yes
Cloud broadband SW albedo	LUT	POLDER	no

Table 1: Summary of proposed products to be implemented as part of the present study.

### 2.2.2 Theoretical basis and heritage for Day-1 cloud properties retrieval algorithms

#### 2.2.2.1 Standalone Cloud Mask

The cloud mask implemented within the POLDER-MODIS processing package has been implemented for 3MI with minimal modifications. This cloud mask relies heavily on the different test developed for POLDER data processing and makes efficient usage of POLDER specific observation but has been enhanced by additional spectral tests thanks to the MODIS extended spectral coverage. This synergistic approach allows in particular to relax a major constraint of the POLDER standalone operational algorithm which depends on a surface bidirectional reflectances atlas built from 10-days syntheses. Thanks to the 3MI higher spatial resolution and extended spectral range (in particular the SWIR spectral domain, including the

high absorption water vapor channel at 1.37 microns), the synergistic POLDER-MODIS cloud mask algorithm, which provides efficient cloud detection with no strong dependency on ancillary data besides traditional meteorological reanalysis (surface pressure, winds, humidity profiles) and digital elevation model, has been directly used with minor changes.

#	Parameter	Test		Condition	Result
01	Apparent pressure	<< surface pressure	Ocean+Land	all	CLOUDY
10	Apparent pressure	~ surface pressure	Ocean+Land		CLEAR
02	Polarized signed reflectance 865nm	< min clear sky	Ocean+Land	all	CLOUDY
03	Polarized signed reflectance 865nm	> 0	Ocean+Land	Out-of-glint Rainbow geometry	CLOUDY
04	Reflectance 865	>> clear sky	Ocean	out-of-glint & snow	CLOUDY
05	Reflectance 865	~< clear sky	Ocean	out-of-glint	CLEAR
06	Reflectance 490	>> clear sky	Land	out-of-glint & snow	CLOUDY
07	Reflectance 490	~< clear sky	Land	out-of-glint	CLEAR
08	Polarized reflectance 490nm – Rayleigh pressure	<< clear sky	Ocean+Land	Out-of-glint No backscattering	CLOUDY
09	Reflectance 865	<<>> reflectance 490	Ocean+Land	out-of-glint	CLEAR
11	Reflectance 1370	> threshold	Ocean+Land	all	CLOUDY
12	Reflectance 1650	< threshold	Ocean	all	CLEAR
13	Reflectances 2130 / 670	> threshold	Land	all	CLEAR
14	Ratio 2130 / 670 and reflectance 443	thresholds	Land	all	CLOUDY
15	Ratio 2130/670, apparent pressure and reflectance 2130	thresholds	Land	all	ICE
16	Ratio 2130/865, apparent pressure and reflectance 2130	thresholds	Ocean	all	ICE

Figure 1: Summary of individual tests implemented for the cloud detection algorithm (Figure courtesy B. Fougnie – Eumetsat)

### 2.2.2.2 Standalone Cloud phase

Initially the PM\_L2 joint processor was developed to implement a synergistic cloud thermodynamic phase retrieval algorithm that infer an index describing cloud phase with different confidence levels ranging from highly confident liquid to highly confident ice, with intermediate levels corresponding to potentially mixed situations (vertical or horizontal mixing, multilayered situation) (Riedi et al, 2010). The algorithm relies on the combination of tests exploiting the multiangle polarization signature of clouds in the VIS/NIR as well as bispectral tests in the VIS/SWIR or TIR range. This algorithm has been directly transposed to process 3MI observations by deactivating the Thermal IR tests and adding additional tests exploiting the polarization signature of clouds in the SWIR range. Note that VII channels could optionally be incorporated in the algorithm to provide information content originally provided by their MODIS equivalent.

Using this synergistic approach it has been demonstrated through comparison to lidar observations (CALIOP) that cloud phase can be correctly identified in 95% of the cases for mono-layered situations and that multilayered situations mainly resulted in “mixed” type or low confidence decision, allowing to distinguish between those situations and the single phase monolayer clouds.

2.2.2.3 *Multilayer cloud detection*

The identification of the monolayer or multilayer character of cloudy scenes is important for satellite retrieval algorithms and for many climate related applications. The presence of multiple layers of clouds may affect significantly the vertical profile of net radiative fluxes and, as a consequence, cloud forcing and feedbacks. A thin top cloud layer may also skew the retrieval of the properties of a cloud at a lower level, as retrieval algorithms are mainly based on the assumption of a single layer cloud. Thus, a mono/multilayer identification might improve the quality of retrieved cloud parameters.

A cloud multilayer flag is part of the last recent version of POLDER/PARASOL products. The algorithm is based upon a decision tree that uses a metric from information theory and a series of tests on POLDER Level-2 products (Desmons et al 2016). The multilayer flag can be used as a confidence in the monolayer and multilayer characters of a scene, or, it can lead to a binary index using a threshold level. Having as reference cloud vertical profiles from active sensors, results show that the binary distinction between monolayer and multilayer scenes is correct for 70% of the cloud scenes (comparable but slightly higher than MODIS inference), and leads to a cloud climatology that exhibits interesting features. This algorithm has been implemented for 3MI using the POLDER/CLOUDSAT/CALIPSO learning database (Figure 2). Future work for improvement of the current implementation would necessitate an optimized learning base for the design of the decision tree tailored for 3MI. The learning database would ideally be composed of 3MI simulated observation for a diverse set of both single layer and multilayered situations.

**Input Criteria to decision tree:**

- Cloud Phase
- AD\_PO2
- PO2 – CTOP
- PO2 – CMOP
- PRAY – PO2
- PRAY
- CTOP
- CMOP

**Final score**

- 0 = full confidence monolayer
- 100 = full confidence multi-layer

(from Desmons et al., 2016)

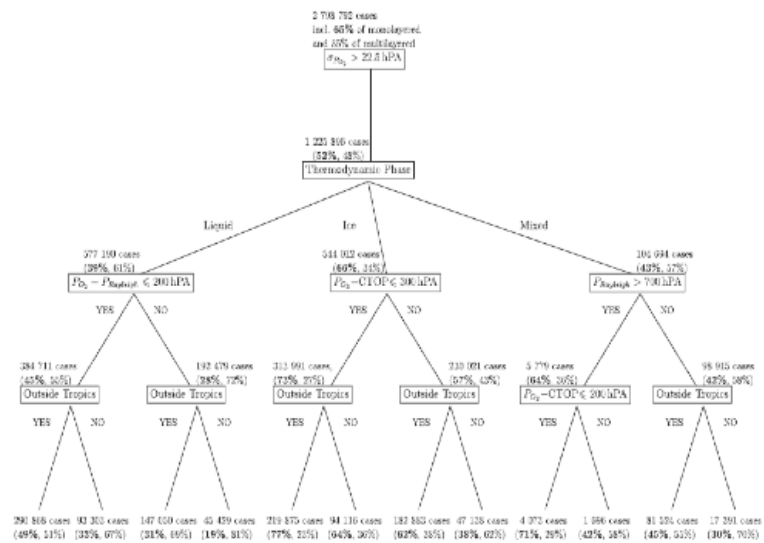


Figure 2: Illustration of the decision tree and input criteria used for multilayered clouds detection.

2.2.2.4 *Baseline cloud vertical extent (altitude and geometrical thickness)*

From the POLDER observations two types of cloud vertical location were historically derived from respectively the spectral variation of molecular scattering polarization signal (the so-called Rayleigh cloud top pressure (Buriiez et al 1997) and the differential absorption in the O2-A band (so-called O2 cloud apparent pressure (Vanbauce et al 1998, 2003). The first one has been established to correspond to cloud top altitude while the second, initially retrieved under assumption that clouds were perfect reflector, was statistically more representative of the pressure at the middle of the cloud.

Although these POLDER products present known shortcomings they also provide significant advantages compare to infrared based techniques (CO<sub>2</sub> Slicing or window channels Brightness Temperature) in specific situations: Rayleigh pressure can be derived without knowledge of atmospheric temperature profile while O<sub>2</sub> A band is insensitive to temperature inversion in lower troposphere as opposed to IR technique. Of even higher interest is the interesting feature that Rayleigh and O<sub>2</sub> A-band cloud pressure tend to diverge significantly in presence of aerosols above clouds as well as for multilayered situation, providing a unique way to identify these situations for further characterization (Waquet et al, 2009; Desmons et al, 2016).

More recently, studies by Ferlay et al (2010) examined the potential of inferring unbiased cloud altitude as well as cloud vertical extent exploiting the multiangular character of POLDER O<sub>2</sub> A-band measurements. Desmons et al (2013) showed, using an intensive statistical comparison with cloud vertical profiles of cloudy columns derived from active sensors, that O<sub>2</sub> apparent cloud pressure could be statistically corrected from in-cloud scattering to retrieve cloud top and middle altitude, and allowing cloud geometrical extend to be retrieved, a first for passive measurements. The CLOVES algorithm developed by Ferlay et al and implemented for operational processing of POLDER data has been implemented for the 3MI cloud prototype software and provides retrieval of Cloud Top Pressure (CTOP), Cloud Middle Pressure (CMOP) as well as two estimates of Cloud Geometrical Thickness (CGT). The first one (CGT\_D) is derived from differences between CTOP and CMOP and the second one (CGT) is inferred from the statistical relation existing between Cloud Geometrical Thickness and the angular variation of the O<sub>2</sub>-A band cloud apparent pressure.

Thanks to the extended 3MI spectral range the Rayleigh cloud top pressure can be derived with higher accuracy as the Rayleigh scattering optical thickness increases rapidly with shorter wavelength. The POLDER algorithm has been transposed to 3MI by using the 410 nm channel instead of the 490 nm currently in use for processing of the PARASOL mission. Also the algorithm has been implemented to use simultaneously 3 channels (410, 670 and 865 nm) to provide a more robust estimate of the Rayleigh optical thickness above cloud from which is derived the Cloud Top Rayleigh pressure (PRAY product).

Finally, although more elaborated retrieval of cloud top altitude and geometrical thickness can be performed using simultaneous inversion of both polarization and O<sub>2</sub> A band channels (see later "Enhanced cloud vertical extent"), the proposed baseline algorithm provides fairly accurate estimate of those parameters while being extremely fast thanks to their analytical and parameterized formulation.

#### *2.2.2.5 Cloud multi-directional optical thickness and particle size from bispectral technique*

Cloud optical thickness is a key parameter for meteorological and climate application. It is widely recognized that its retrieval can suffer from significant biases linked to cloud horizontal heterogeneity and 3D effects. Providing several estimates of cloud optical thickness from the 3MI multiview observations is by itself an interesting information in order to evaluate cloud physical models assumption (plane parallel ? Links between radiative and microphysical properties). It also provides a much stronger constraint for instantaneous radiances to flux conversion as the cloud bidirectional reflectance function (BRDF) is sampled under different geometries which allow to either compute weighted average of directional parameters or even select those geometries that are expected to be less sensitive to 3D effects.

While the POLDER algorithm used a single cloud particle size and habit for either liquid or ice cloud optical thickness retrieval, 3MI will allow simultaneously the retrieval of cloud particle size by implementing the commonly used Nakajima & King (1990) bispectral technique.

The POLDER cloud optical thickness algorithm already implemented uses precomputed look-up tables which have been adapted to cover the extended 3MI spectral range and the simple minimization technique yields a fast algorithm that can quantify uncertainties associated to retrieved parameters thanks to the multiple view estimates. It should be noted that such uncertainty estimates remain mostly inaccessible to other instruments which have to rely on single view measurements to characterize clouds.

An multiangle implementation of the Nakajima & King method has been implemented for COT and CER retrieval using Look-Up tables providing a fast yet performant retrieval algorithm as will be illustrated and discussed in following sections.

#### *2.2.2.6 Liquid cloud effective particle size from polarization (optional)*

An optimal estimation approach has been implemented to retrieve liquid cloud effective radius from multi-angle polarization measurements at full resolution 3MI pixel scale, improving over the original implementation by Breon and Goloub (1998) by simultaneously considering the 3 POLDER polarized channels (490, 670 and 865 nm) and accounting for realistic measurements errors.

This algorithm currently relies on precomputed look-up tables and is fast enough to operate under NRT constraints. It currently uses only the 3 visible channels (490, 670 and 865 nm) but can be easily extended to make use of the 3MI longer wavelength channels at 1.6 and 2.1 micrometers. Because polarization is mainly created by single scattering events, it is expected that consistent retrievals can be obtained from these additional channels without having to account for vertical variability of cloud properties. The retrieved particle size will be representative of liquid droplets at cloud top and will complement the other values retrieved from bi-spectral approach.

#### *2.2.2.7 Cloud visible narrow-band and shortwave broadband albedo*

As a by-product of the retrieved cloud optical thickness/particle size, and assuming plane parallel clouds, the narrow band spectral cloud albedo is obtained for 3MI channels at 443, 670 and 865nm. Buriez et al (2005, 2007) developed for POLDER an algorithm that derives the broadband shortwave albedo assuming those three spectral values could be representative of the spectral intervals 0.2 - 0.55  $\mu\text{m}$ , 0.55 – 0.7  $\mu\text{m}$  and 0.7 - 4  $\mu\text{m}$  respectively. Using a simple parametrization, spectral albedo are used to infer cloud shortwave broadband albedo. For 3MI a similar approach has been implemented.

It should be noted that 3MI narrow-band and shortwave albedo products have been implemented only for cloudy pixels but the algorithm might be easily extended over clear sky scenes at a later stage. Also, future work could focus on incorporating the new 3MI SWIR channels to provide a more accurate spectral integration.

## 3 Description of the 3MI-CLD-L2 processing software

### 3.1 Prototype software main functions and logical workflow

A full framework has been developed to allow efficient processing of 3MI L1C and testing of proposed algorithms. This prototype software is based on the POLDER-MODIS processing package that has been developed during several years at LOA for analysis of combined POLDER and MODIS observations within the A-Train. It has a fully modular architecture and provides all ancillary data needed to perform state of the art cloud properties retrieval (surface properties dynamic atlas, ECMWF meteorological fields from reanalysis, handling of large LUT, flexible I/O procedures for easily reading various input and writing output products, traceability of runtime parameters, ...). This package has been adapted to handle 3MI L1C data as input and internal pixel information structures were also adapted to 3MI observations. Following this, the retrieval modules implemented for POLDER-MODIS processing have been modified to account for 3MI new observations characteristics but with minimal work required in terms of software functionalities.

The processing prototype software implemented is structured according to workflow diagram illustrated in Figure 3.

The processing logic is organized according to the following steps :

- Processing is instantiated by the **main** function
- Reading in and initialization of processing parameters (input files, libraries, ..) is made through setup of **System Parameters**
- All **Look-up Tables** required by the retrieval modules are initialized and loaded
- **Output File** is instantiated and created on disk for output during processing
  
- **Loop** over available **granules** (L1C file)
  - o **Loop** over all **overlaps** available within each granule
    - Creation of Output Overlap within Output File
    - **Loop** over **Pixel**
      - Read in Input pixel information from input file
      - Create and initialize Output pixel structure
      - Sequentially apply for all valid pixels
        - o Atmospheric profile module
        - o Gaseous absorption module
        - o Scene Pressure module
        - o Cloud detection module
        - o Water Vapor content module
        - o Sequentially apply for all cloudy pixels
          - Cloud Phase module
          - Cloud Rayleigh Pressure module
          - Cloud Droplet Radius (liquid - polarization) optional module
          - Cloud Top Pressure
          - Cloud Middle Pressure
          - Cloud Multilayer Flag
          - Cloud Geometrical Thickness
          - Cloud Optical Thickness
          - Cloud Effective Radius (ice/liquid - bispectral)
          - Cloud Oxygen Pressure
          - Cloud Broadband Shortwave Albedo
        - o True Color Composite optional module
      - **End Loop** : Write Pixel to Output Overlap
    - o **End Loop** : Write Output Overlap to Output File
  - **End Loop** : Write/Close Output File
  
  - Deallocate all

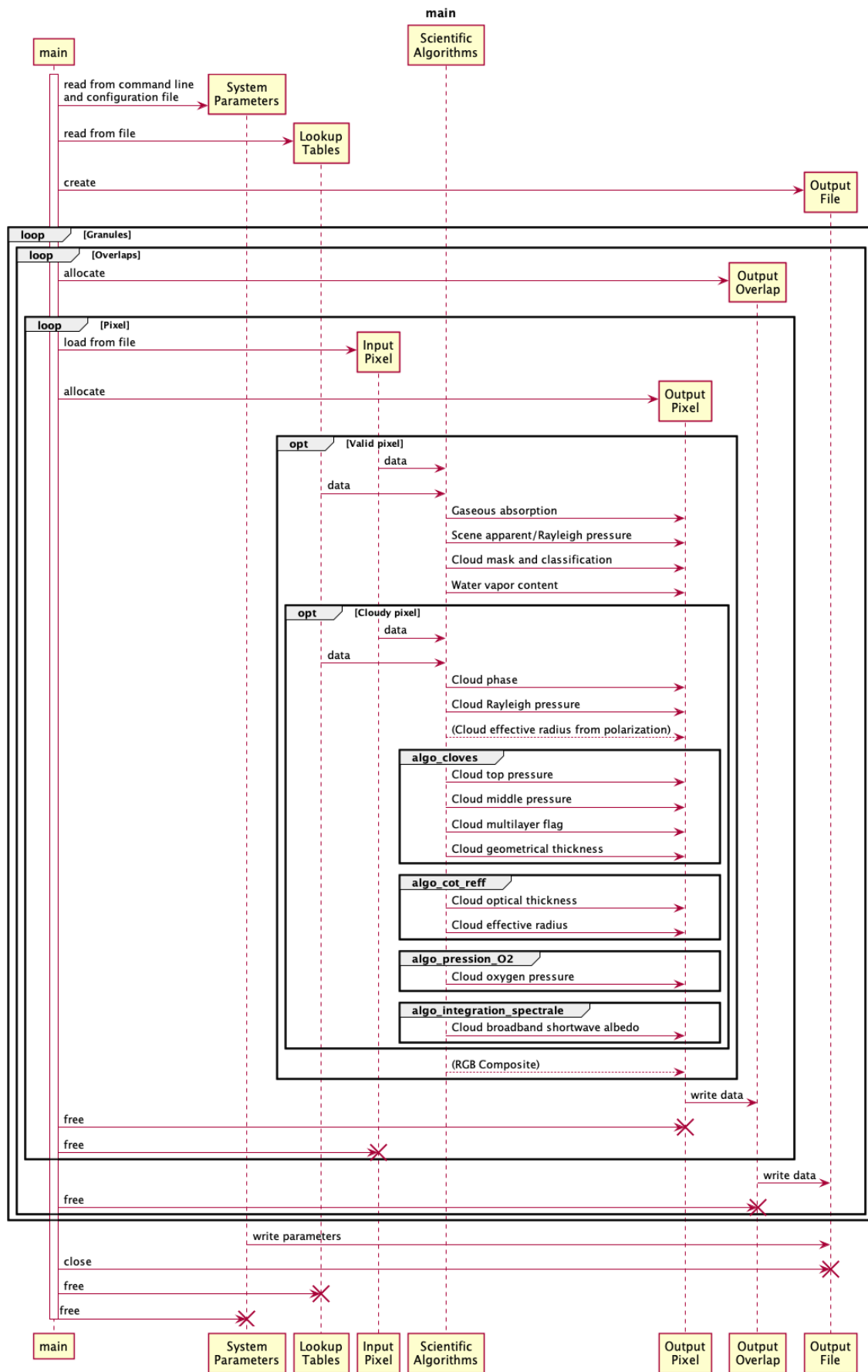


Figure 3: Schematic diagram of the prototype code structure, main functions and logical workflow.

## 3.2 Current status of algorithm implementation

### 3.2.1 List of implemented products

We provide hereafter in Table 2 and Table 3 a list of currently implemented algorithm and retrieved products. For reference the science module name within the delivered prototype software is also provided in Table 3.

Product	Symbol	Units / Classes	Valid Range	Directional/Pixel
Cloud mask	CMask	Classes : confident clear, probably clear, probably cloudy, confident cloudy	0 - 3	Pixel
Cloud Phase	CP	Confidence index 0 = confident liquid 200 = confident ice	0 - 200	Pixel
Multilayer flag	MLF	probability	0 - 100	Pixel
Cloud Optical thickness	COT	unitless	0 - 100	DIR / Pixel
Effective size from bispectral (ice and liquid)	CER	$\mu\text{m}$	2 – 30 (liquid) 2 – 100 (ice)	Pixel (DIR optional)
Droplet effective radius (liquid only) from polarisation	CER_POL	$\mu\text{m}$	2 - 30	Pixel
Rayleigh cloud top pressure	PRAY	hPa	20 - 1050	DIR / Pixel
O2-A band cloud pressure	PO2	hPa	20 - 1050	DIR / Pixel
Cloud Top Pressure	CTOP	hPa	20 - 1050	Pixel
Cloud Middle Pressure	CMOP	hPa	20 - 1050	Pixel
Cloud Geometrical Thickness	CGT	km	0 - 20	Pixel
Cloud Geometrical Thickness (delta CTP / CMP)	CGT_D	Km	0-20	Pixel
Cloud spectral albedo	ASVIS	unitless	0 – 1.0	Pixel
Cloud broadband SW albedo	ASW	unitless	0 – 1.0	Pixel
Column Water Vapor Content	WVC	$\text{g.cm}^{-2}$	0.1 – 10	Pixel

Table 2: Summary of implemented products along with units and expected valid range.

### 3.2.2 Evaluation of NRT compatibility

The entire products set described in Table 3 can be generated from the prototype software for a data granule containing 2 L1C overlaps (corresponding to ~1 min of 3MI observation) within 4 min on average using 1 core (Intel(R) Xeon(R) CPU E5-2670 0 @ 2.60GHz) and 5 Gb of RAM.

Considering most modern CPUs nowadays provide easily 18 cores and share RAM space of several tens of gigabytes, the prototype software therefore allows to conclude that implemented algorithms are fully (with vast margins) compatible with Near Real Time processing.

Product long name	Dataset name	Science module reference name
Cloud Mask	cloud_classification	algos/cloud_detection/src/mmm_sci_cloud_detection.c
Cloud Phase	cloud_phase	algos/cloud_phase_detection/src/mmm_sci_cloud_phase_detection.c
Multilayer Flag	mlf	algos/solver/br2/src/albedo_cot.f90 :subroutine algo_cloves
Cloud Optical Thickness	cot	algos/solver/br2/src/albedo_cot_reff.f90 :subroutine algo_albedo_cot_reff
Cloud Effective Particle size	reff	algos/solver/br2/src/albedo_cot_reff.f90 :subroutine algo_albedo_cot_reff
Rayleigh cloud top pressure	cloud_rayleigh_pressure	algos/cloud_rayleigh_pressure/src/mmm_sci_cloud_rayleigh_pressure.c
O2-A band cloud pressure	poxy	algos/solver/br2/src/albedo_cot.f90 :subroutine algo_pression_O2
Cloud top pressure	ctop	algos/solver/br2/src/albedo_cot.f90 :subroutine algo_cloves
Cloud middle pressure	cmop	algos/solver/br2/src/albedo_cot_reff.f90 :subroutine algo_albedo_cot_reff
Geometrical thickness (DeltaP)	h_deltap	algos/solver/br2/src/albedo_cot.f90 :subroutine algo_integration_spectrale
Geometrical thickness (AD PO2)	h_adpoxy	algos/water_vapor_content/src/mmm_sci_water_vapor_content.c
Cloud spectral albedo	asvis	algos/cloud_detection/src/mmm_sci_cloud_detection.c
Cloud broadband SW albedo	asw	algos/cloud_phase_detection/src/mmm_sci_cloud_phase_detection.c
Integrated water vapor content	water_vapor_content	algos/solver/br2/src/albedo_cot.f90 :subroutine algo_cloves

Table 3 : List of Day-1 products available from the 3MI\_L2-Cloud prototype software, corresponding short name of the product dataset within output file and reference to relevant source code.

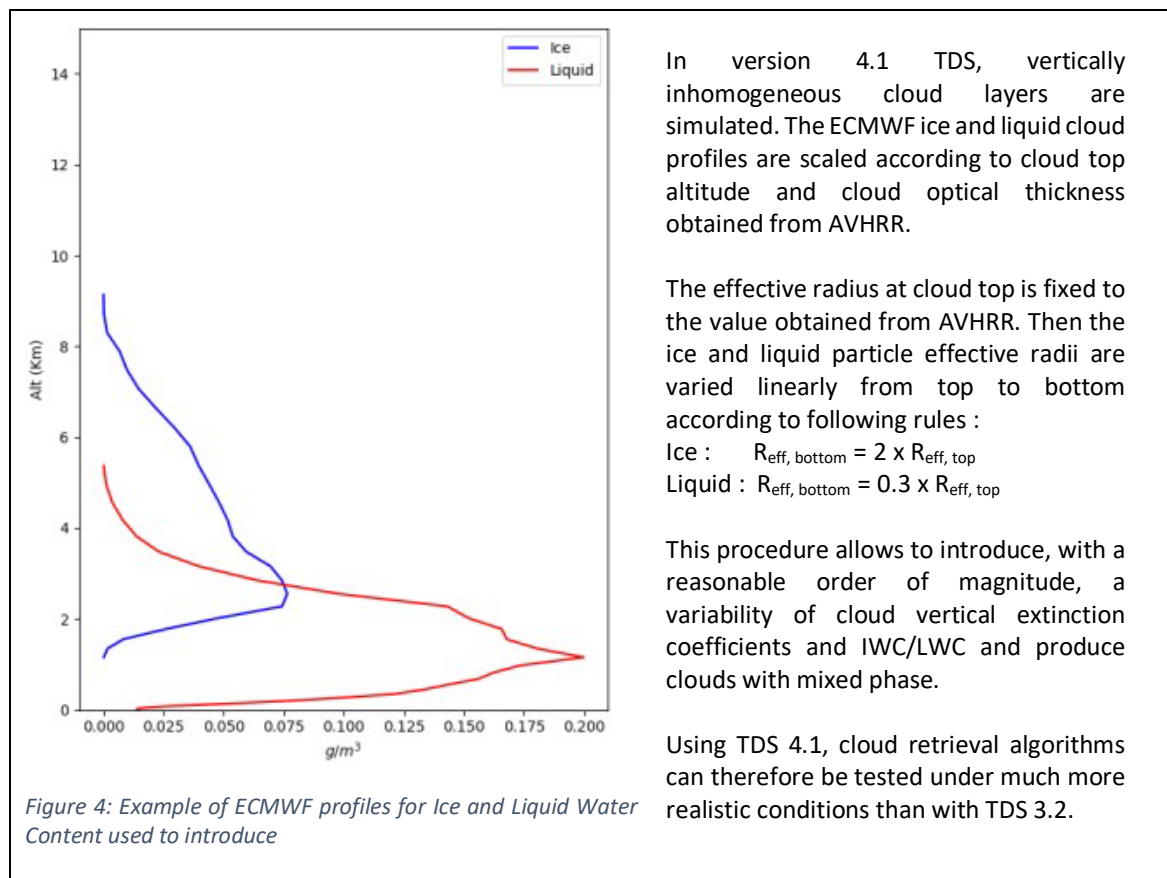
## 4 Assessment of retrieved properties

### 4.1 General approach

A synthetic dataset consisting of one orbit has been created to obtain synthetic 3MI data of varying complexity. Evaluation of the algorithms performances has been made by comparing retrieved values to the corresponding parameters used as simulation inputs.

Two flavors of test data with different complexity have been produced:

- Test data set 3.2: clouds are defined as plane/parallel, homogeneous, single phase and of fixed geometrical thickness (particle size, altitude and optical thickness will vary). In addition no aerosols are incorporated in cloudy skies, while aerosols are also described using a single model and profile for any given clear sky pixel.
- Test data set 4.1: clouds have been simulated assuming much more complex assumptions. Cloud layers have varying geometrical thickness, can be multilayered, they can contain both liquid and ice phase for any given layer and aerosols are also distributed vertically through the atmospheric allowing for aerosol above clouds situations. ECMWF profiles are used to describe vertical variation of particle size and extinction (see Figure 4 for example and details).



The validation results presented hereafter are based on processing of 3MI L1C test data versions 3.2 and 4.1 for the orbit covering parts of Europe and Africa on 23 February 2008.

## 4.2 Specifics for comparison of retrievals against V3.2 and V4.1 input parameters

Comparing retrieved values against input parameter used to describe cloud layers in TDS V3.2 is fairly straightforward since cloud layers are assumed to be homogeneous hence described using single values. The only exception is the cloud mask product which is provided as 4 categories: confident clear, probably clear, probably cloudy and confident cloudy. Hereafter, confident and probably clear pixels will be considered as clear, whereas confident and probably cloudy pixels are considered as cloudy.

For the vertically heterogeneous cloud layers with varying vertical profiles of particle size, extinction coefficient and phase the comparison become significantly less trivial as a single number can not capture the vertical distribution of those parameters. In order to allow for a one-to-one comparison, we have adopted an approach whereby the input cloud properties are averaged vertically top-down from cloud top over a given part of the profile depending on the expected penetration depth of channels used in the retrieval. For instance, it is well known that polarization signal tends to saturate as optical thickness reaches a value of  $\sim 2.0$  (exact value depending on details such as microphysics, geometrical extent, ...) while a technique relying on thermal infrared bands will be most sensitive to the signal arising for the first unit of optical depth from cloud top. This is illustrated by Figure 5 where it is clear that the phase mask derived from ECMWF profile (center and right images) clearly depends on how much of the cloud top layer is considered when computing the average ice fraction. On that example, the AVHRR phase product derived from thermal infrared channels, is much more consistent with the information contained with the first unit of optical depth (center) rather than what can be derived when considering a thicker part of the top cloud layer (right). For the 3MI phase product that is inferred from a combination of polarization and SWIR observation, we will consider the first two units of optical depth.

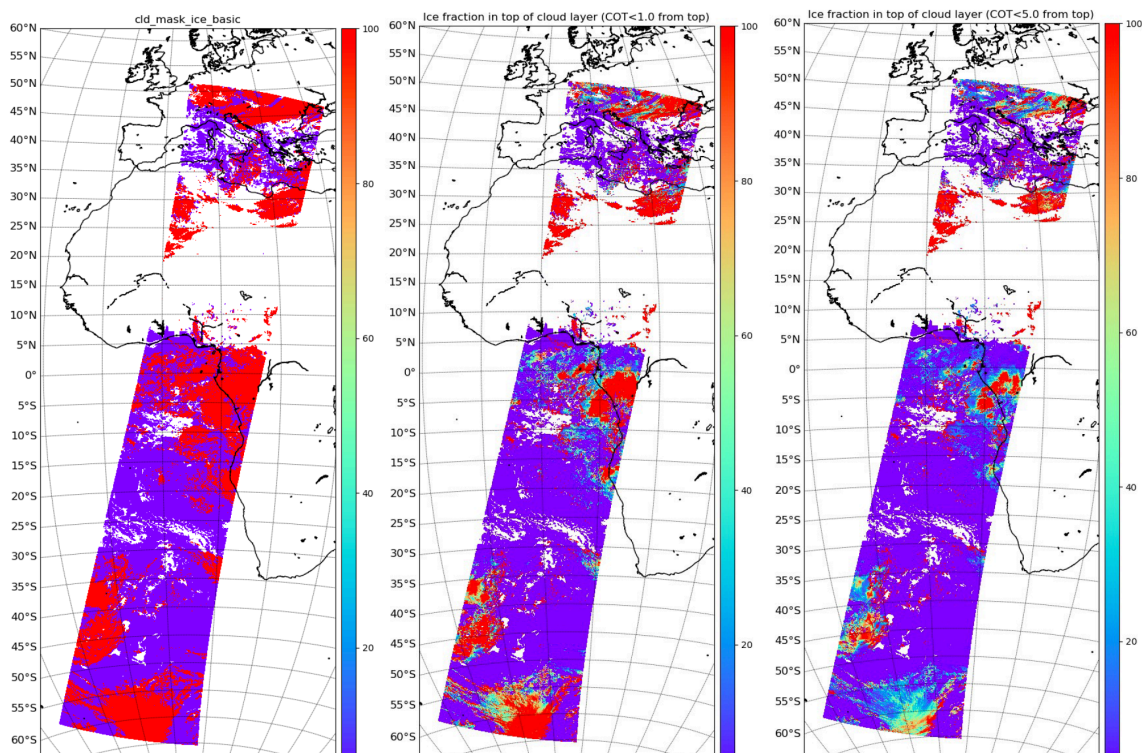


Figure 5: Comparison between the AVHRR binary (ice/liquid) phase mask used for TDS V3.2 simulation (left) and the ice fraction computed from ECMWF reanalysis when integrating the IWC/LWC vertical profiles down to an optical depth of 1.0 (center) or 5.0 (right).

On the other end, the SWIR channels used for cloud particle size retrievals have a deeper penetration depth and the weighting functions associated to those channels (Platnick, 2000) tend to peak deeper within the cloud. This is illustrated by Figure 6 where we compared the retrieved particle effective radius to the average value obtained when integrating cloud particle size profiles from cloud top down to an optical depth of 1.0 (left), 5.0 (center) and 10 (right). The best agreement is clearly obtained when considering an integration depth of 5.0, consistent with the SWIR channel weighting function as estimated by Platnick (2000).

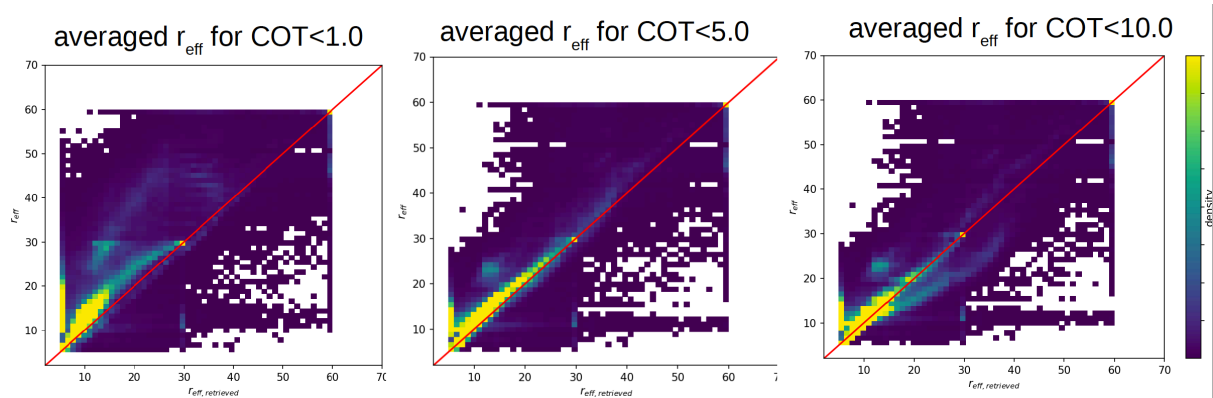


Figure 6: Comparison of retrieved effective radius with average value obtained when integrating cloud particle size profiles from cloud top down to an optical depth of 1.0 (left), 5.0 (center) and 10 (right).

Comparison between retrieved cloud top and actual end of cloud top profile is also subject to specific situation depending on sharpness of transition between cloudy and clear atmosphere. In that case, a common assumption is that passive retrievals of cloud top height from thermal infrared channels are representative again of the altitude of the top layer extending over the first unit of optical depth. Specific techniques might have different penetration depth and it has been shown from POLDER that Rayleigh derived pressure is very close to cloud top while O2-A band apparent pressure derived from differential absorption have a much larger penetration depth and tend to correspond to cloud middle pressure. For consistency with cloud top pressure products derived from infrared channels (such as VII cloud products) we will compare in the following our cloud top pressure retrieval (output of the CLOVES module) with the pressure level corresponding to the middle of the first unit of cloud optical depth determined from input ECMWF profiles specified for test data simulation.

Finally, multilayer situation will be identified in input data when the vertical separation between the peak of the IWC profile and the peak of the LWC profile is greater than 500 m.

Table 4 summarizes the assumption made for translation of TDS V4.1 input vertical profiles into single values that can be compared with retrieved parameters.

Retrieved Parameter	Assumption
Cloud Phase	Dominant fraction of ice or liquid within integrated top 2.0 optical depth
Cloud Effective Radius	Averaged Reff within integrated top 5.0 optical depth
Cloud Top Height	Pressure level at the middle of the first 1.0 optical depth
Multilayer Mask	Geometrical separation between Max(IWC) and Max(LWC) > 500 m

Table 4: Summary of rules applied to convert vertical profile information used in TDS V4.1 into single value parameter.

## 5 Results for V3 Test data

### 5.1 Cloud Detection

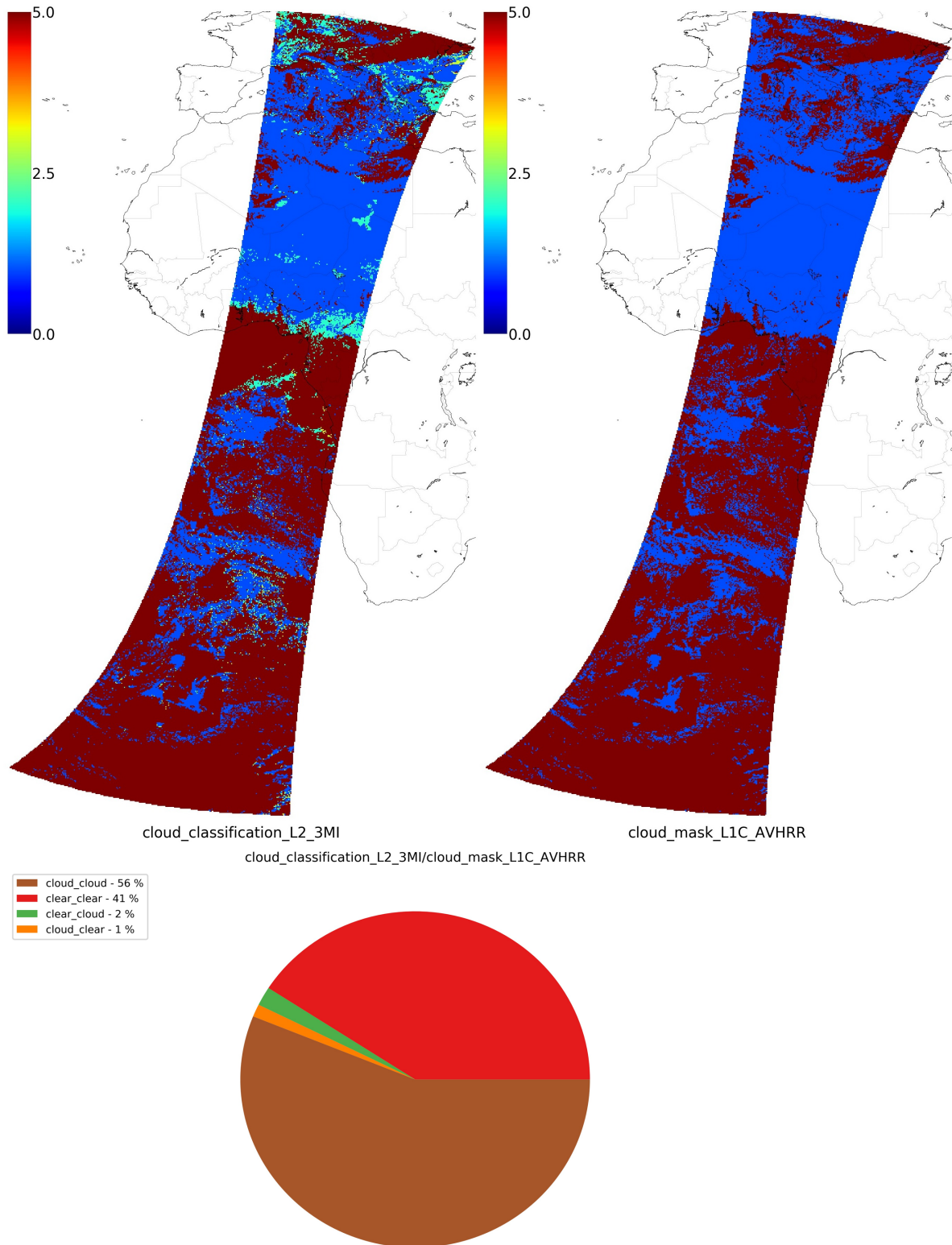


Figure 7 : Example of cloud mask detection (top left) against assumed AVHRR Cloud Mask (top right) and classification scores (bottom)

### 5.2 Cloud Thermodynamic Phase

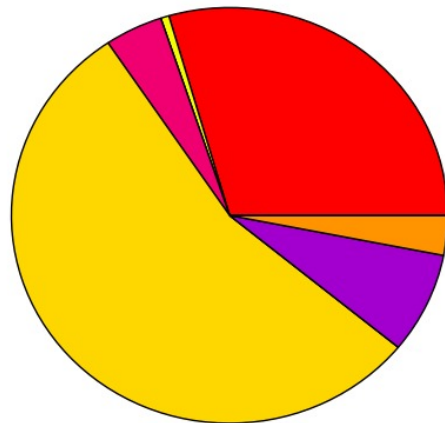
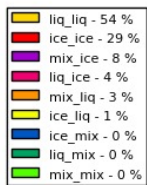
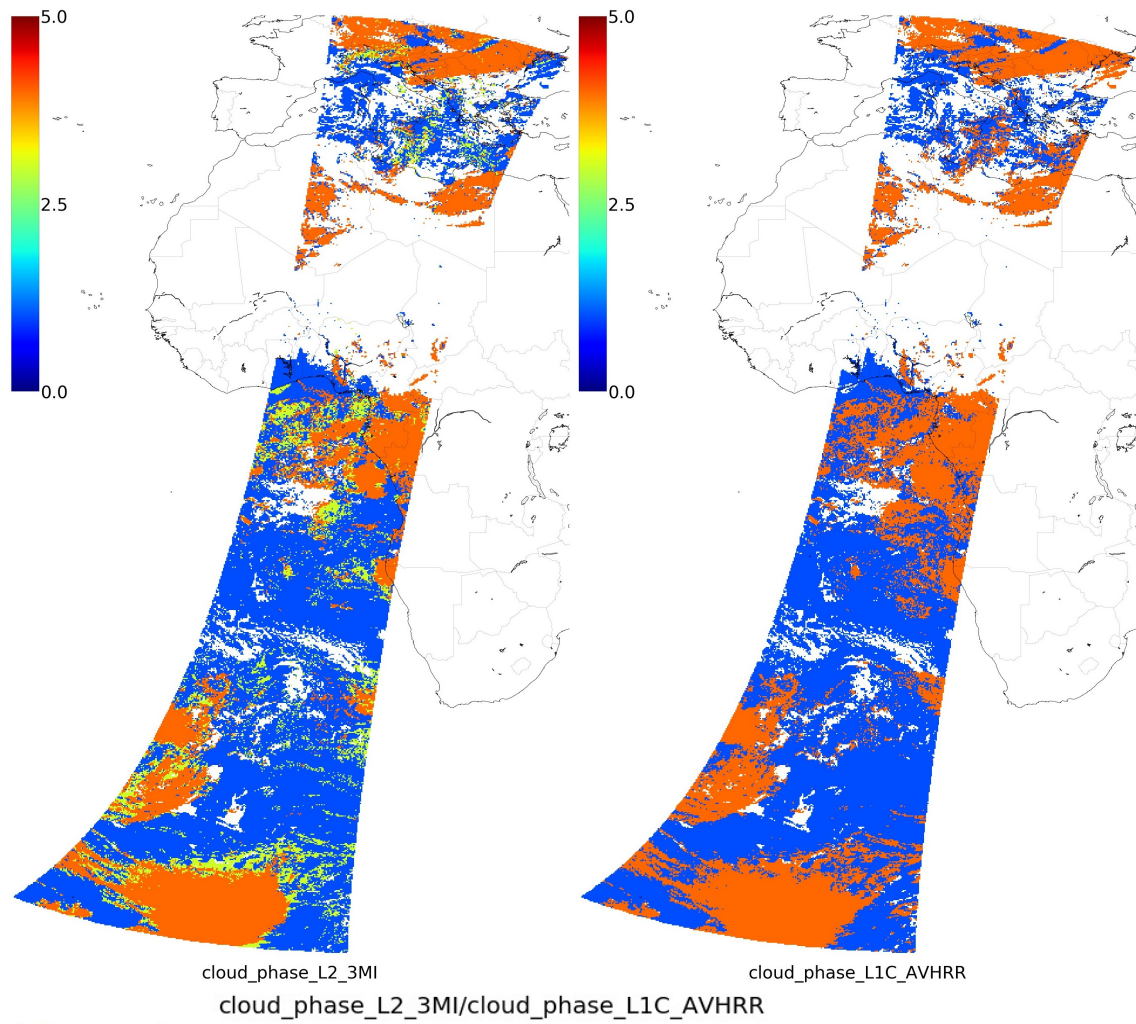


Figure 8 : Example of cloud phase detection (top left) against assumed AVHRR Cloud phase (top right) and classification scores (bottom).

### 5.3 Cloud Top Pressure from Rayleigh signal and O2-A band Scene Apparent Pressure

#### 5.3.1 Examples

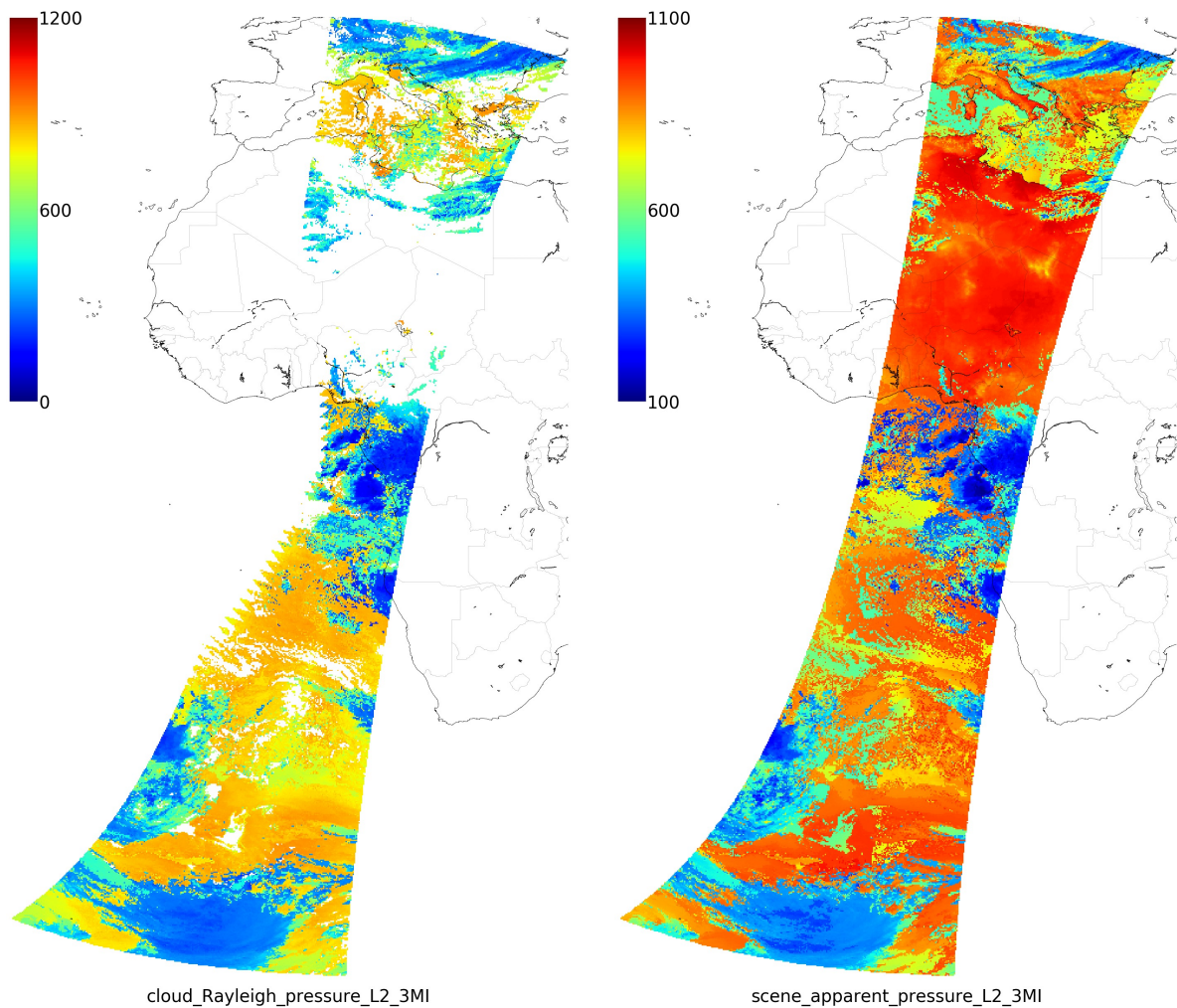
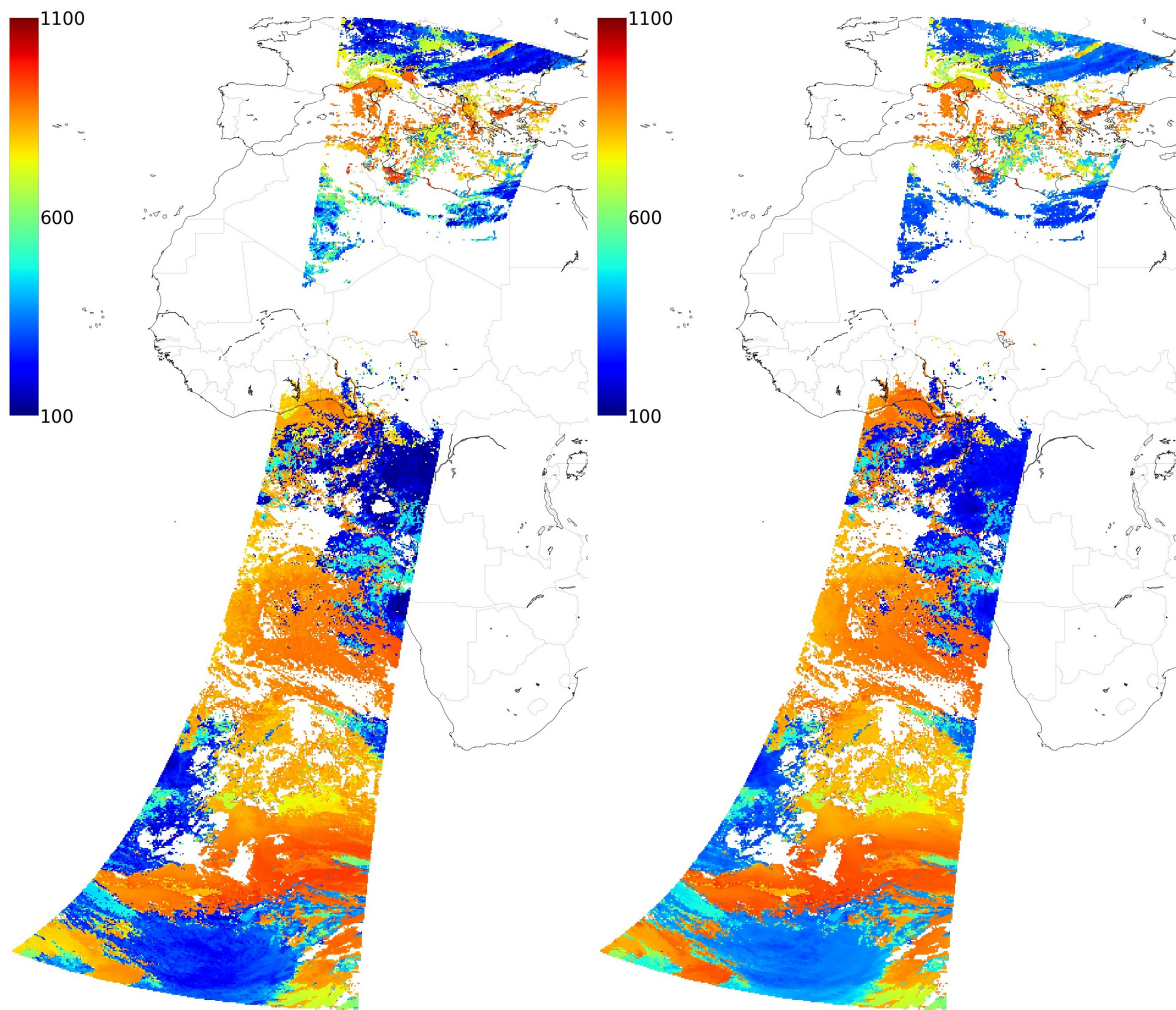


Figure 9: Example of cloud top pressure retrieved from polarization Rayleigh scattering signal and scene apparent pressure from O2-A band differential absorption.

5.4 Cloud Top Pressure from O2-A band

5.4.1 Global Comparison



cloud\_oxygen\_pressure\_top\_L2\_3MI

cld\_height\_acha\_L1C\_AVHRR

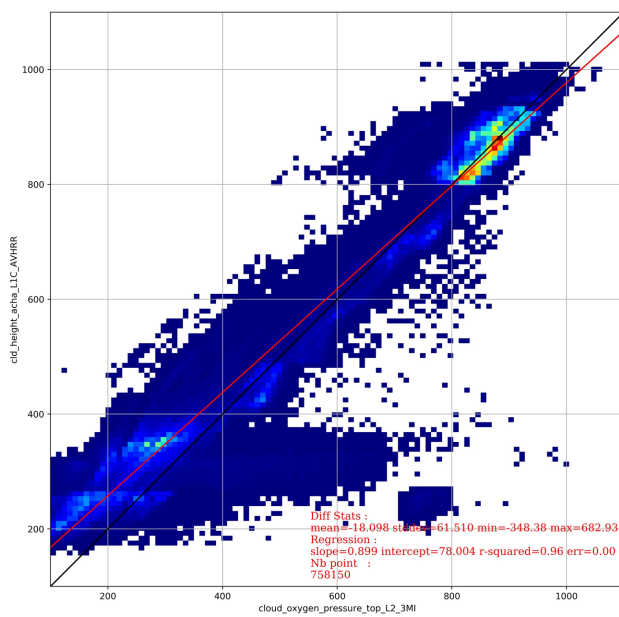


Figure 10 : Cloud top pressure retrieved from O2-A band algorithm (CLOVES output – top left) against assumed AVHRR cloud top pressure (top right) along with global comparison scatterplot (bottom left).

5.4.2 Comparison by cloud phase

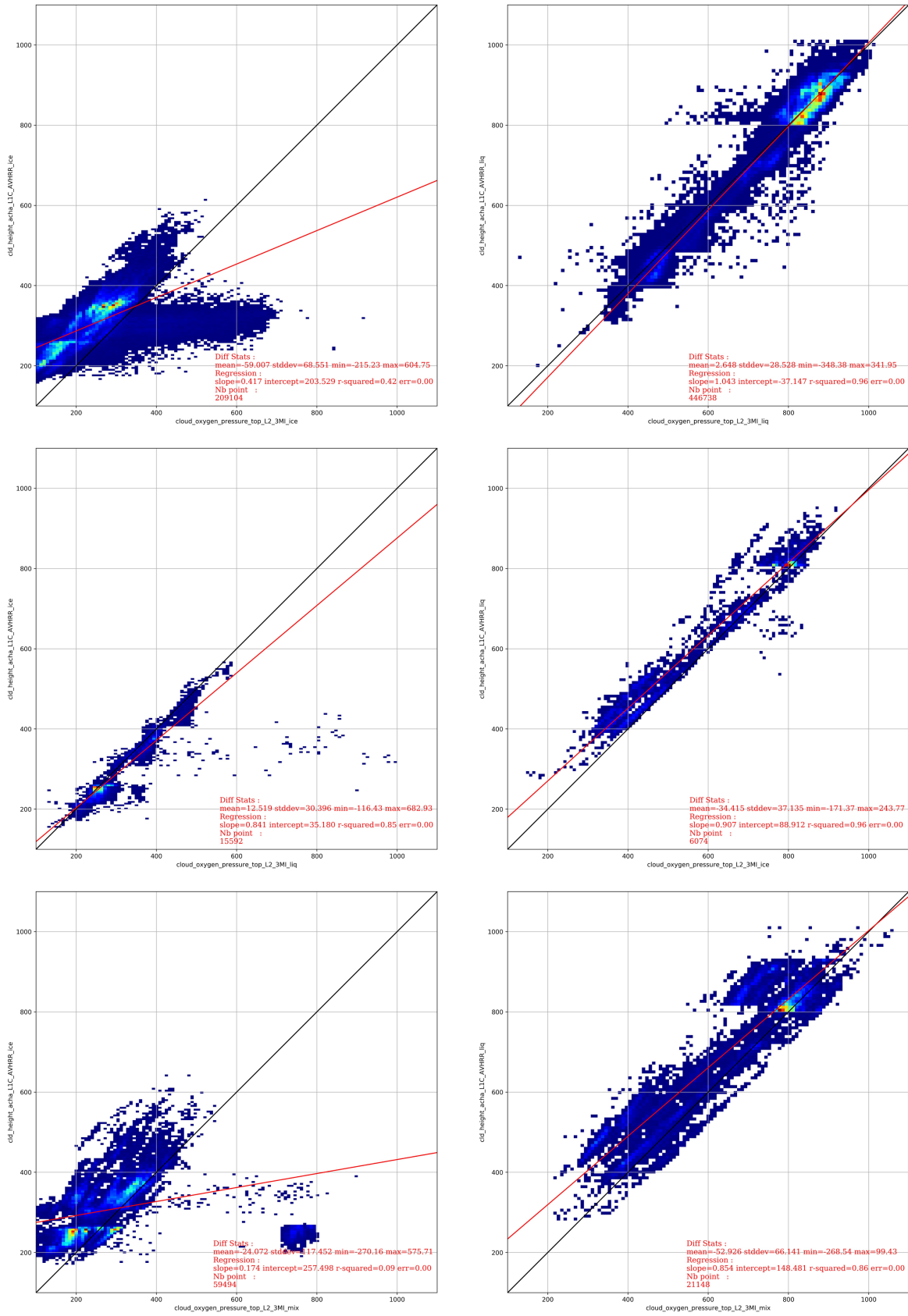


Figure 11 : Comparison between O2-A band retrieved and assumed cloud top pressure for different categories of retrieved and assumed cloud phase.

## 5.4.3 Cloud Apparent pressure &amp; Cloud Middle Pressure from O2-A band

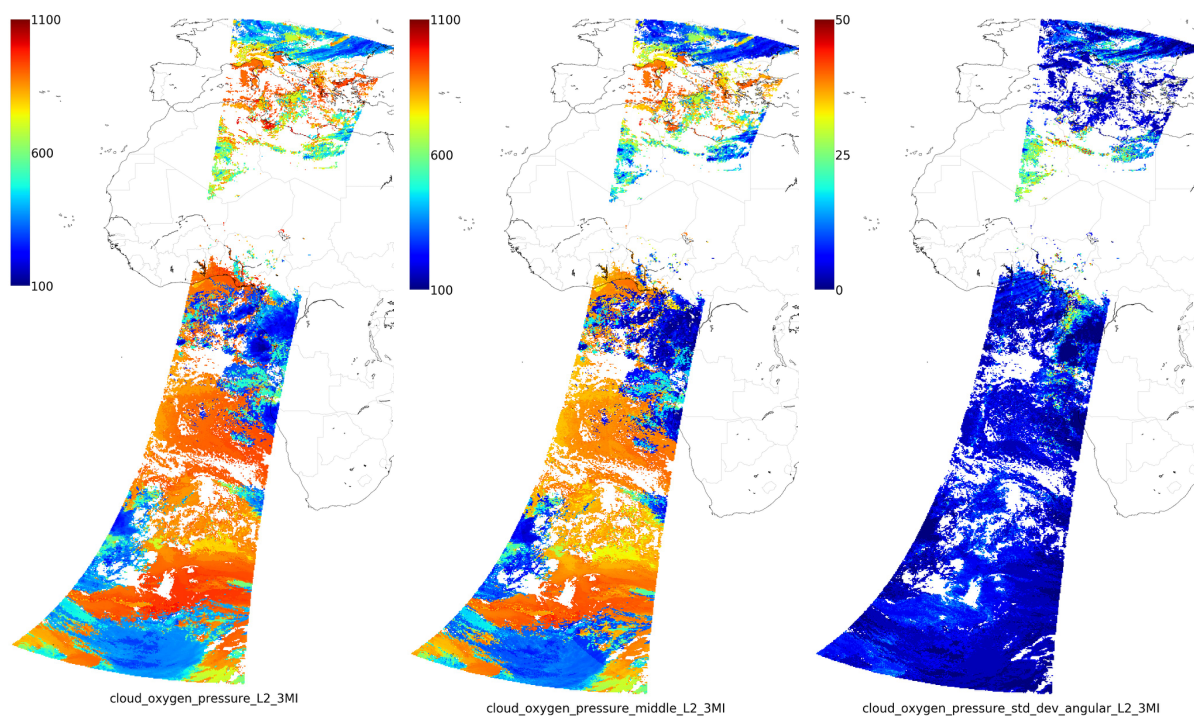


Figure 12: Example of Cloud Apparent Pressure (derived from O2-A band – left), cloud middle pressures (CLOVES algorithm estimate) and standard deviation of the multiangle retrievals of Cloud Apparent Pressure

## 5.5 Cloud Geometrical Thickness

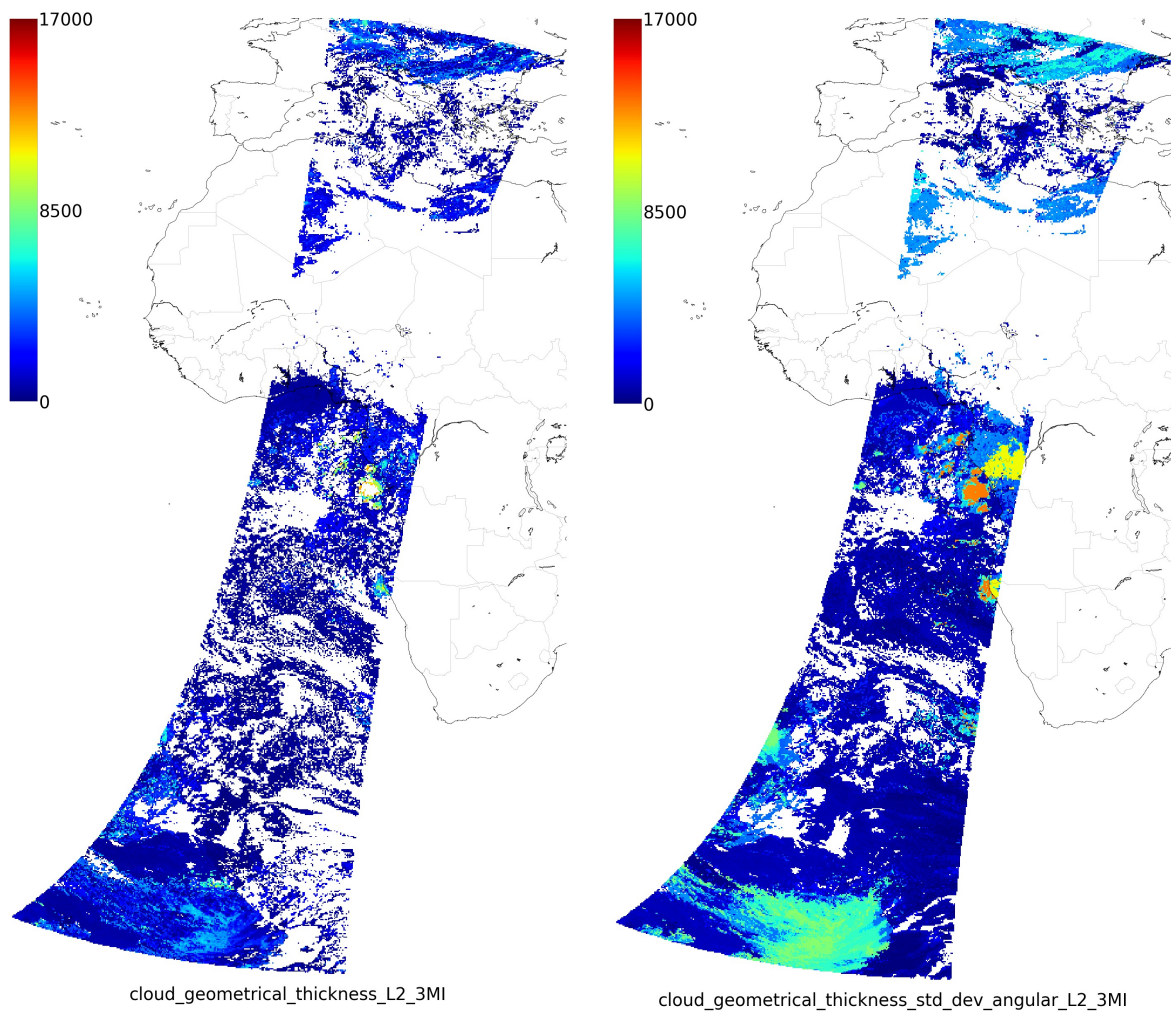
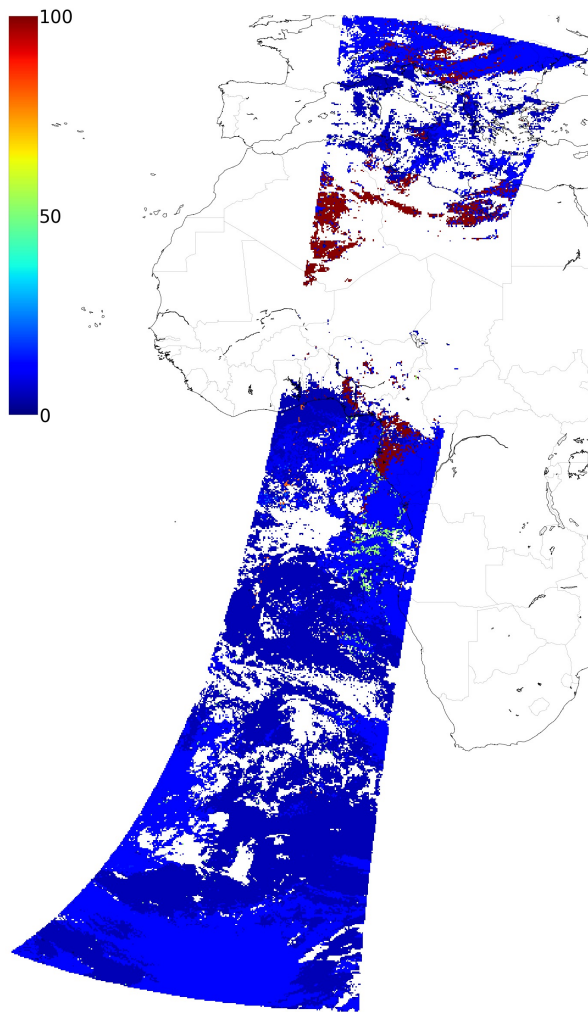


Figure 13: Cloud geometrical thickness retrieved from Cloud Top and Cloud Middle Pressure (left) and Cloud Geometrical Thickness inferred from standard deviation of the multiangle O2-A band cloud apparent pressure retrievals.

## 5.6 Multilayered Clouds Occurrence



cloud\_multi\_layer\_flag\_L2\_3MI

Figure 14 : Example of multilayer flag output from the multi-layered cloud detection algorithm. Here for TDS V3.2, the probability of multilayer situation is low everywhere due to single cloud layer assumptions.

## 5.7 Cloud Optical Thickness

### 5.7.1 Global Comparison

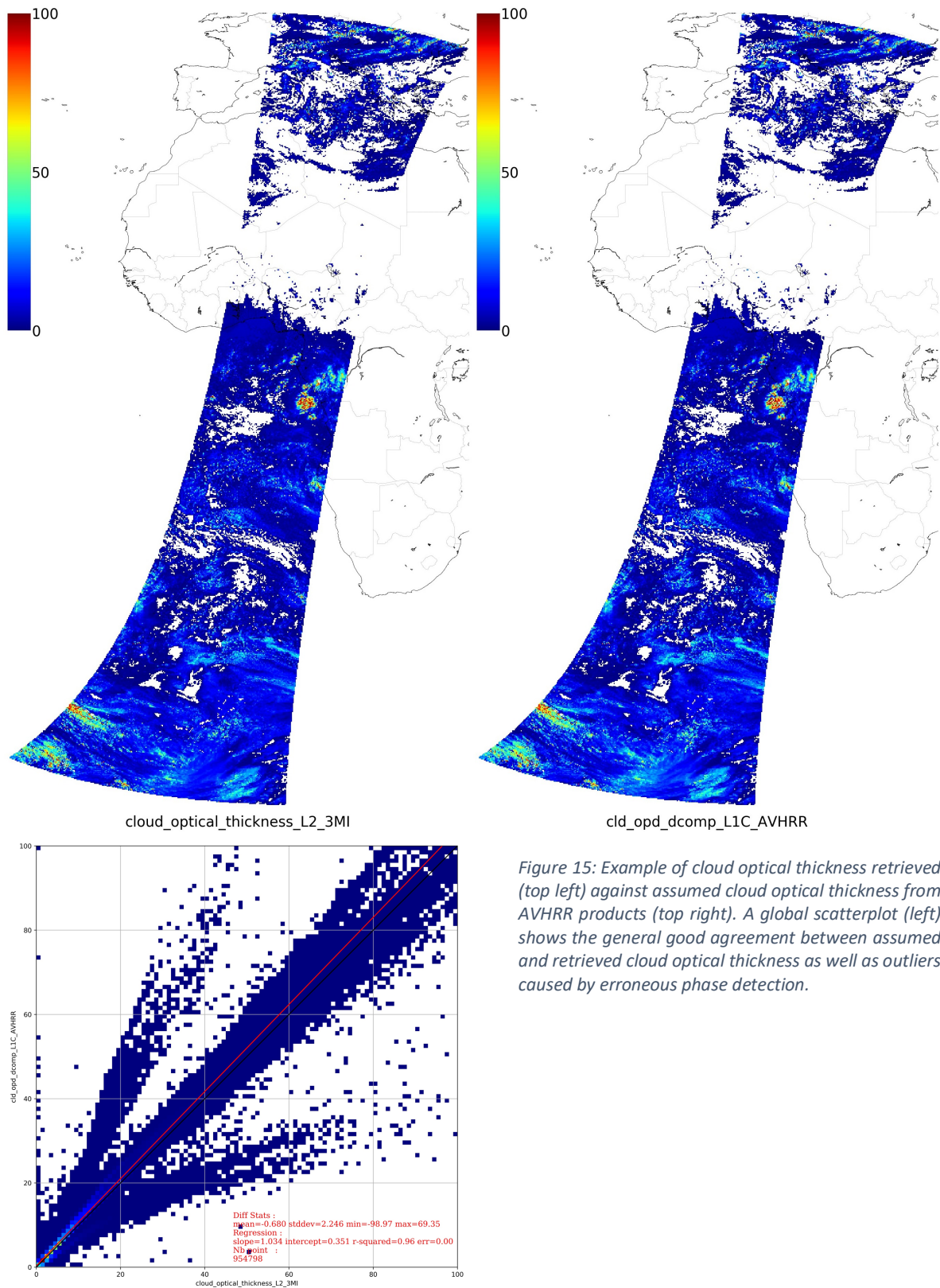


Figure 15: Example of cloud optical thickness retrieved (top left) against assumed cloud optical thickness from AVHRR products (top right). A global scatterplot (left) shows the general good agreement between assumed and retrieved cloud optical thickness as well as outliers caused by erroneous phase detection.

5.7.2 Comparison by cloud phase

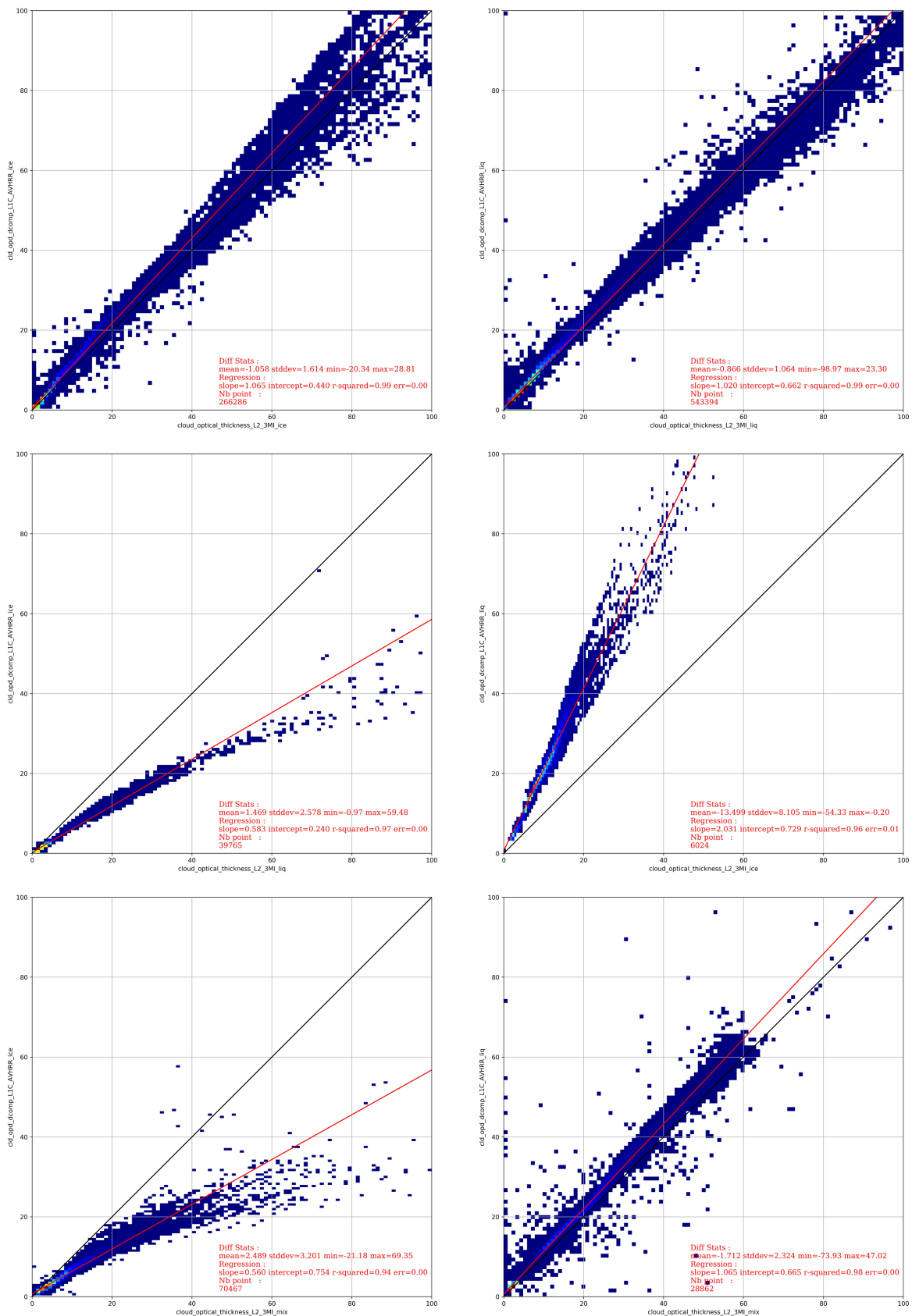


Figure 16 : Scatterplots of assumed against retrieved cloud optical thickness for different combinations of assumed/retrieved cloud top phase. Agreement between retrieved and assumed optical thickness is generally very good when cloud phase can be determined consistently, while erroneous phase assumptions lead to systematic biases in cloud optical thickness retrievals.

5.8 Cloud Particle Effective Radius

5.8.1 Global Comparison

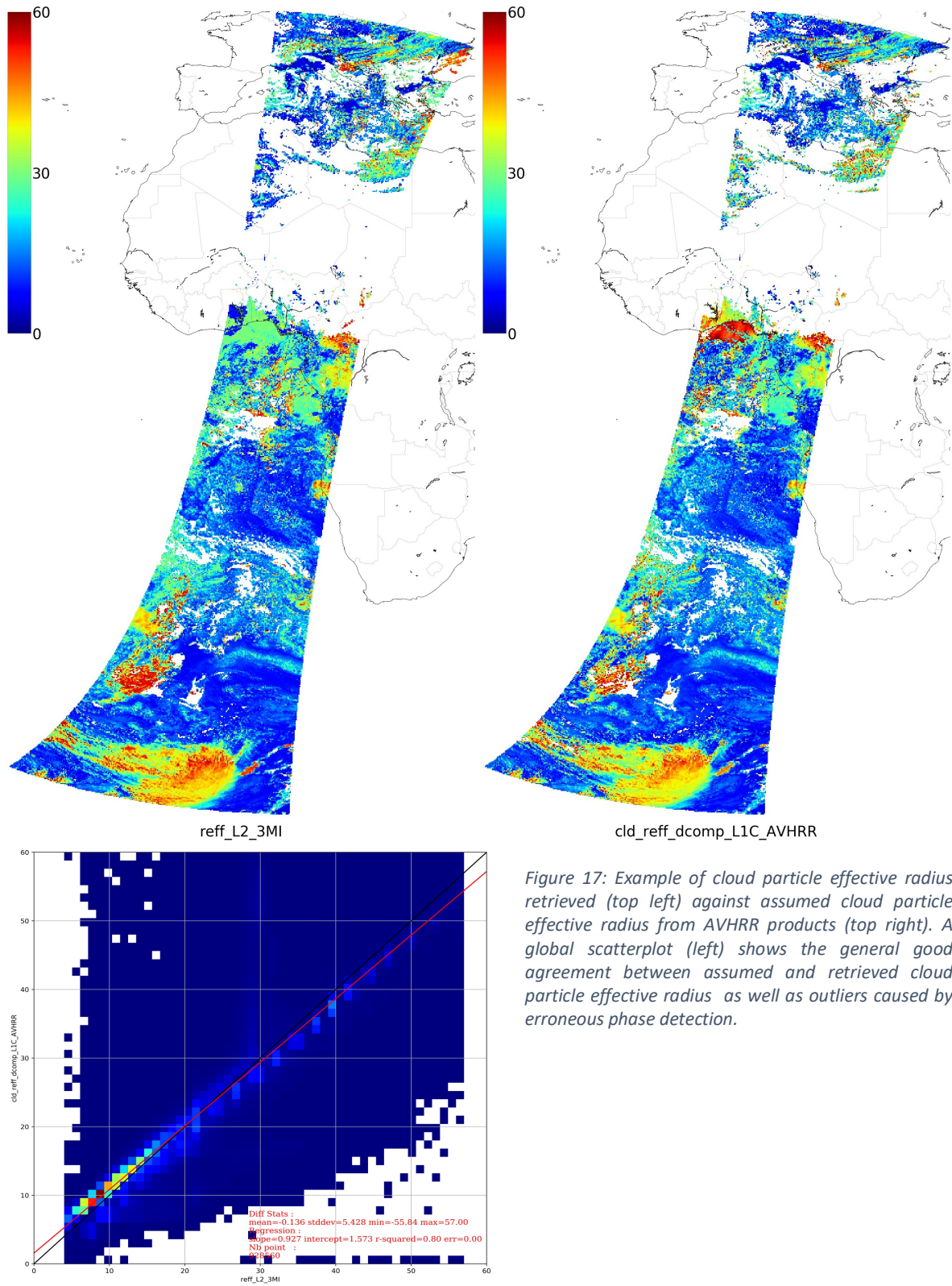


Figure 17: Example of cloud particle effective radius retrieved (top left) against assumed cloud particle effective radius from AVHRR products (top right). A global scatterplot (left) shows the general good agreement between assumed and retrieved cloud particle effective radius as well as outliers caused by erroneous phase detection.

5.8.2 Comparison by cloud phase

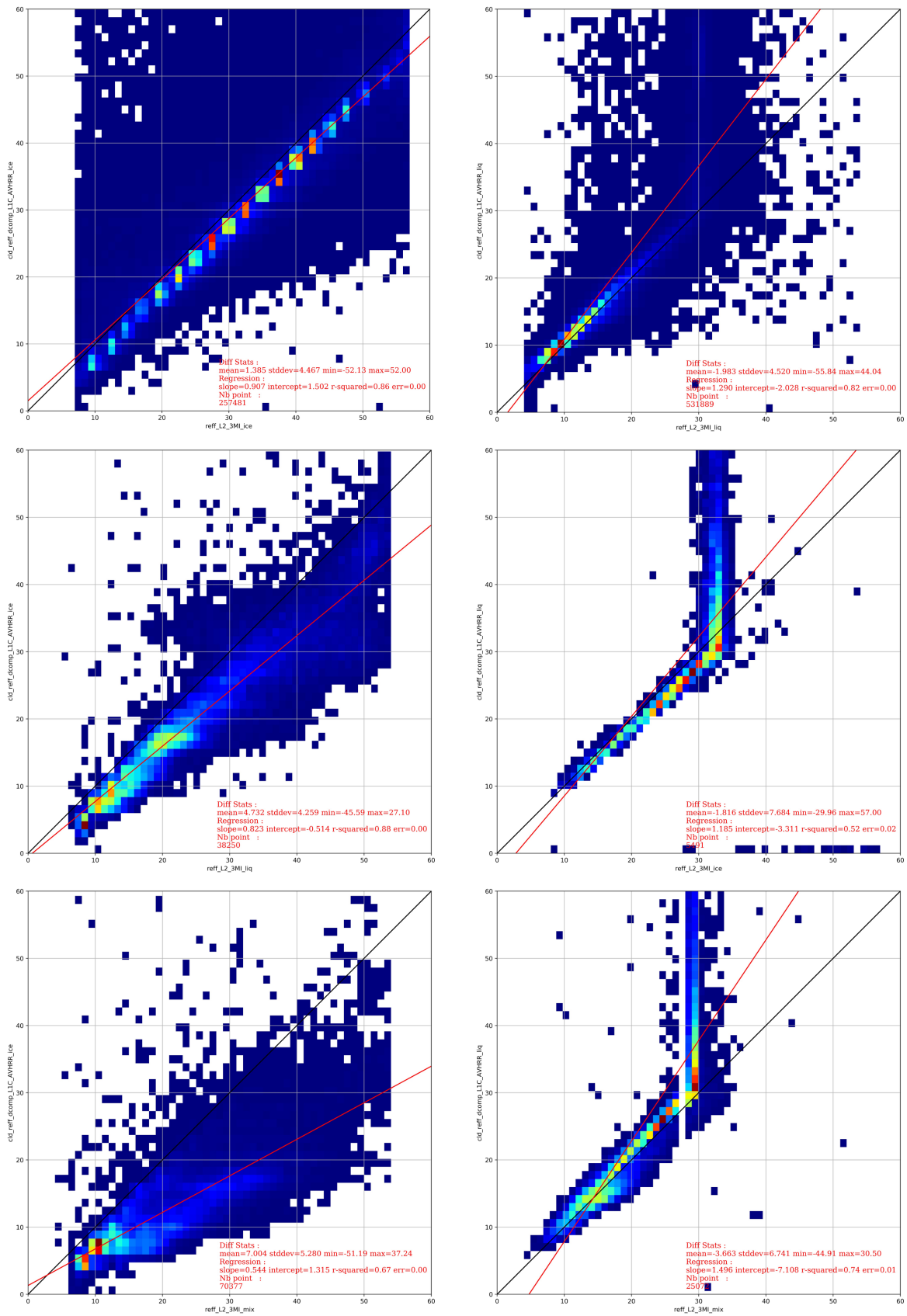
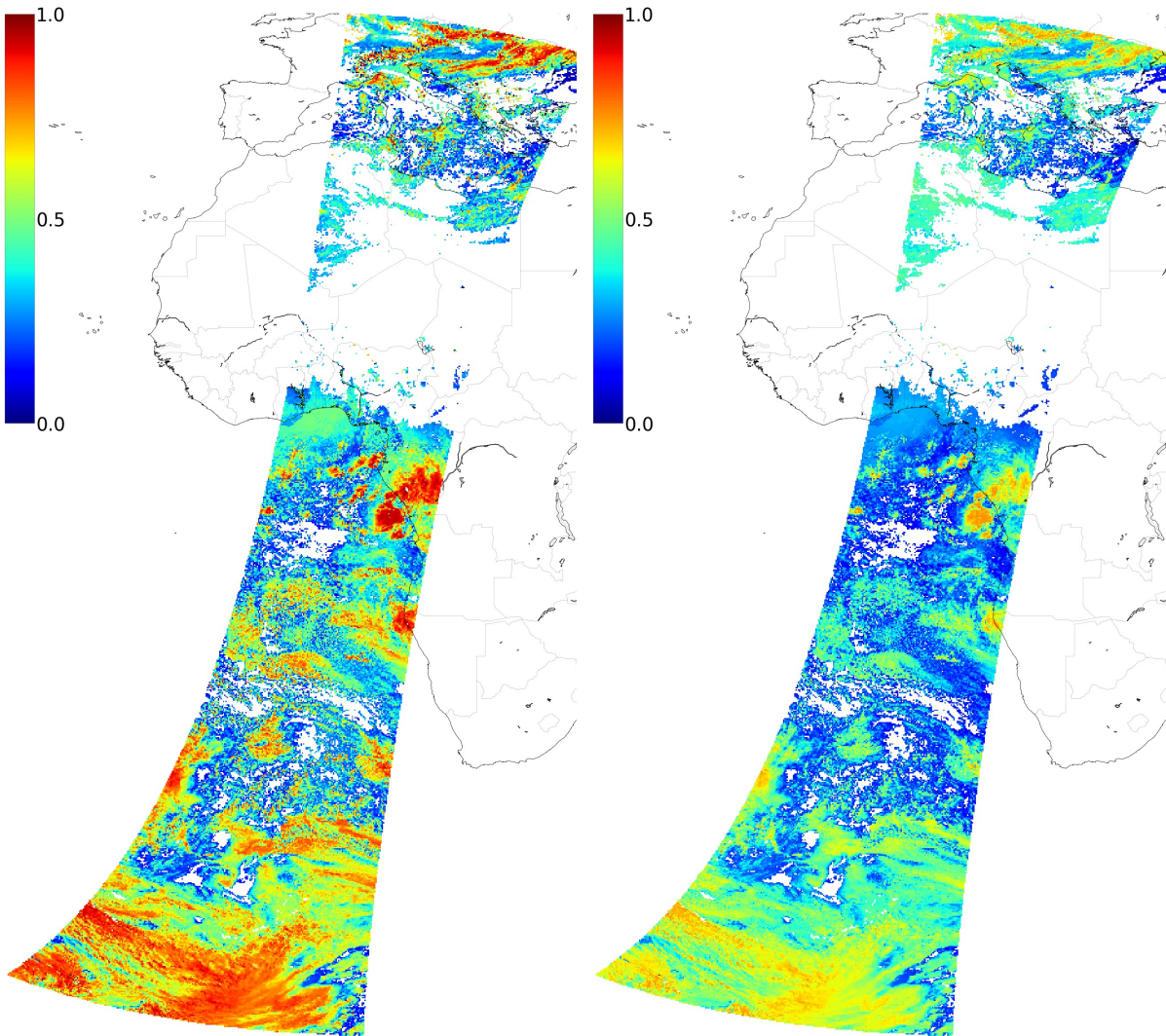


Figure 18 : Comparison between assumed and retrieved cloud particle effective radius for different combination of retrieved/assumed cloud phase. Agreement is generally good when cloud phase detection agrees with assumed optical properties used for test data simulation.

5.9 Cloud Spherical Albedo & Shortwave Albedo

5.9.1 Examples



cloud\_spherical\_albedo\_VIS\_L2\_3MI

albedo\_SW\_L2\_3MI

Figure 19: Example of Cloud Spherical Albedo and integrated Shortwave Albedo products retrieved from Test Data Set V3.0

## 6 Results for V4 Test data

### 6.1 Cloud Detection

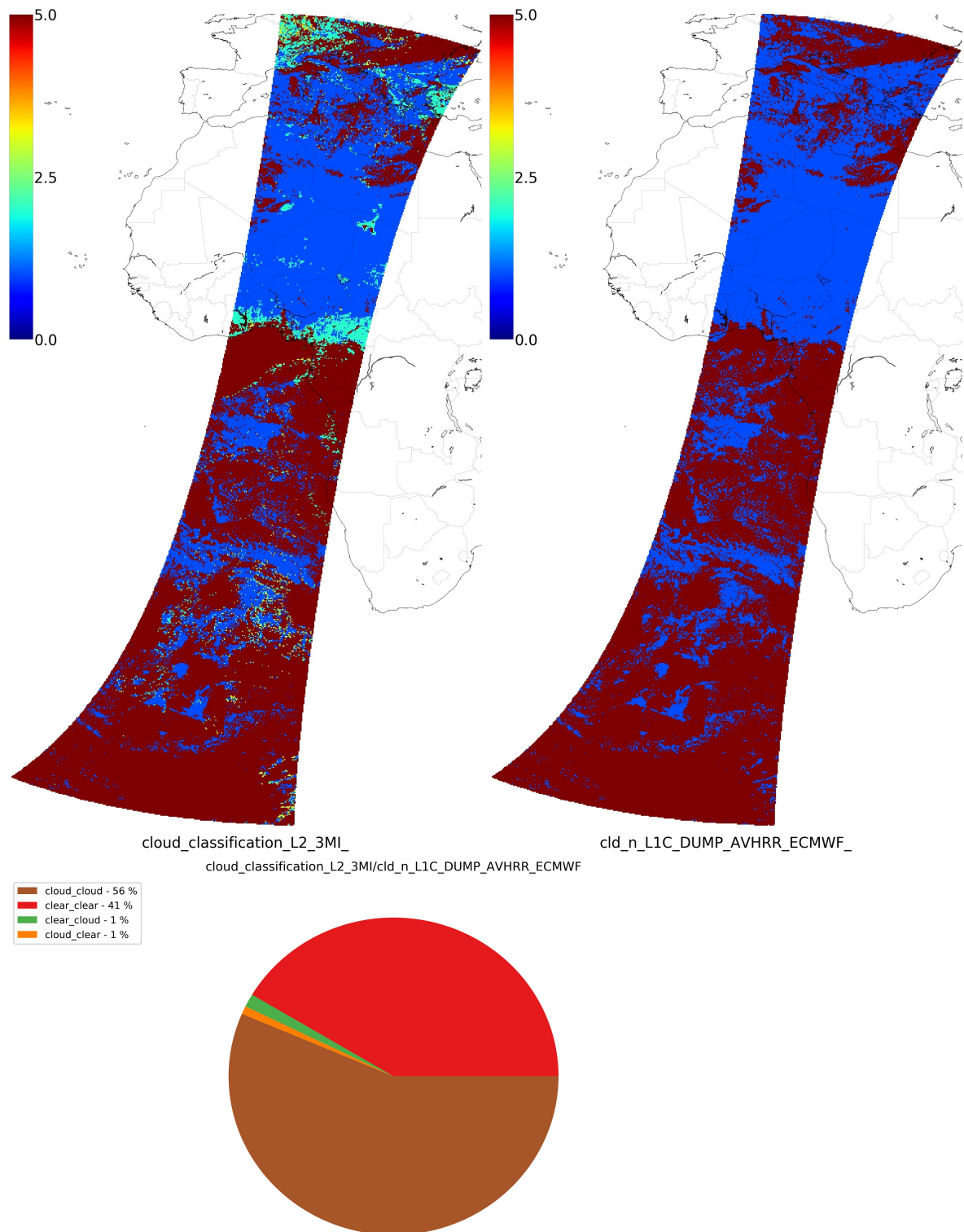


Figure 20 : Example of cloud mask detection (top left) against assumed AVHRR Cloud Mask (top right) and classification scores (bottom).

## 6.2 Cloud Thermodynamic Phase

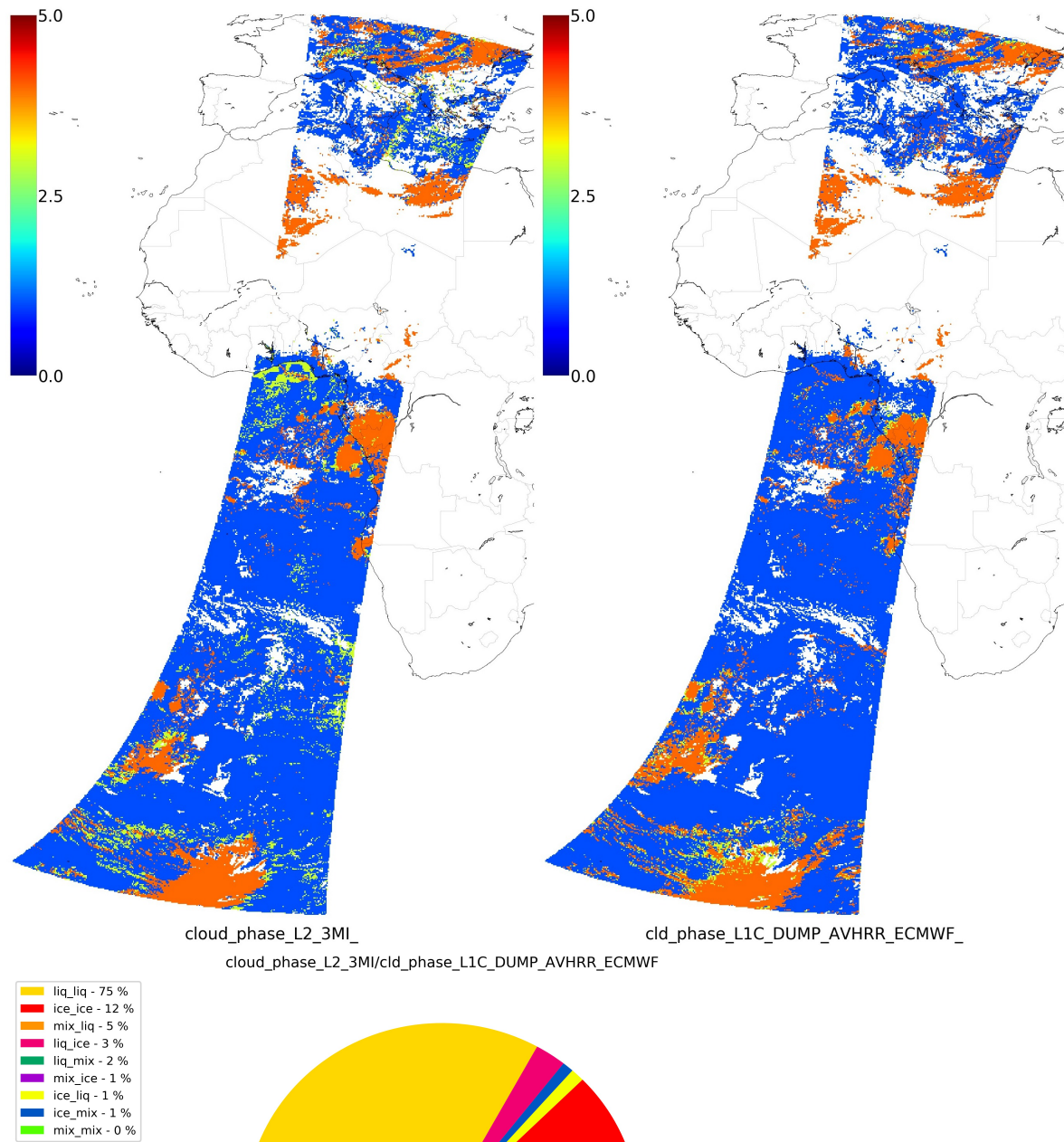
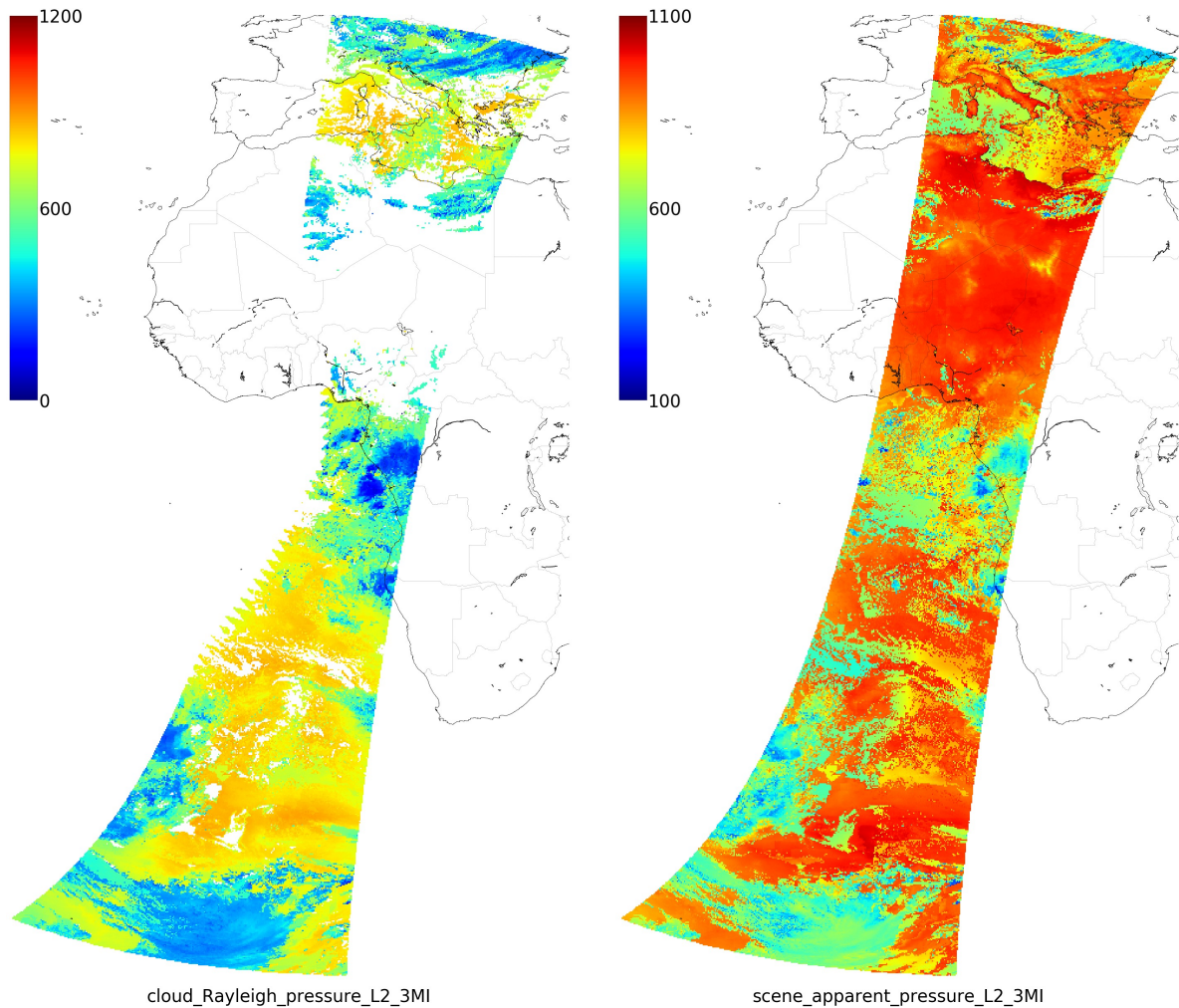


Figure 21 : Example of cloud phase detection (top left) against assumed ECMWF Cloud phase (top right) and classification scores (bottom).

### 6.3 Cloud Top Pressure from Rayleigh signal and O2-A band Scene Apparent Pressure

#### 6.3.1 Examples



cloud\_Rayleigh\_pressure\_L2\_3MI

scene\_apparent\_pressure\_L2\_3MI

Figure 22: Example of cloud top pressure retrieved from polarization Rayleigh scattering signal and scene apparent pressure from O2-A band differential absorption.

6.4 Cloud Top Pressure from O2-A band

6.4.1 Global Comparison

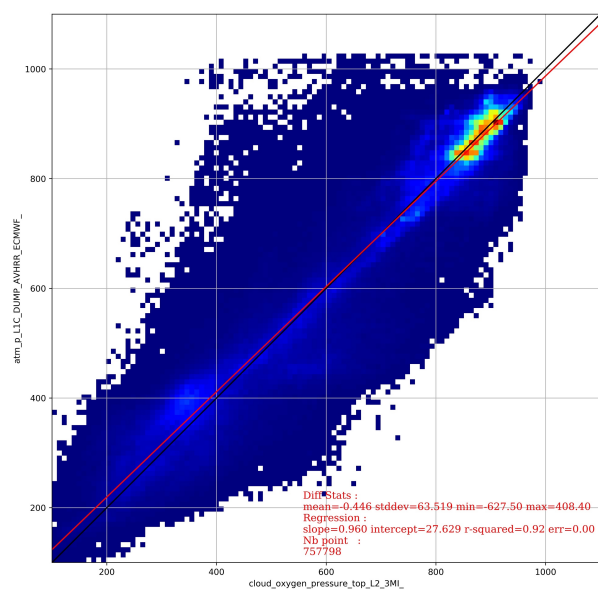
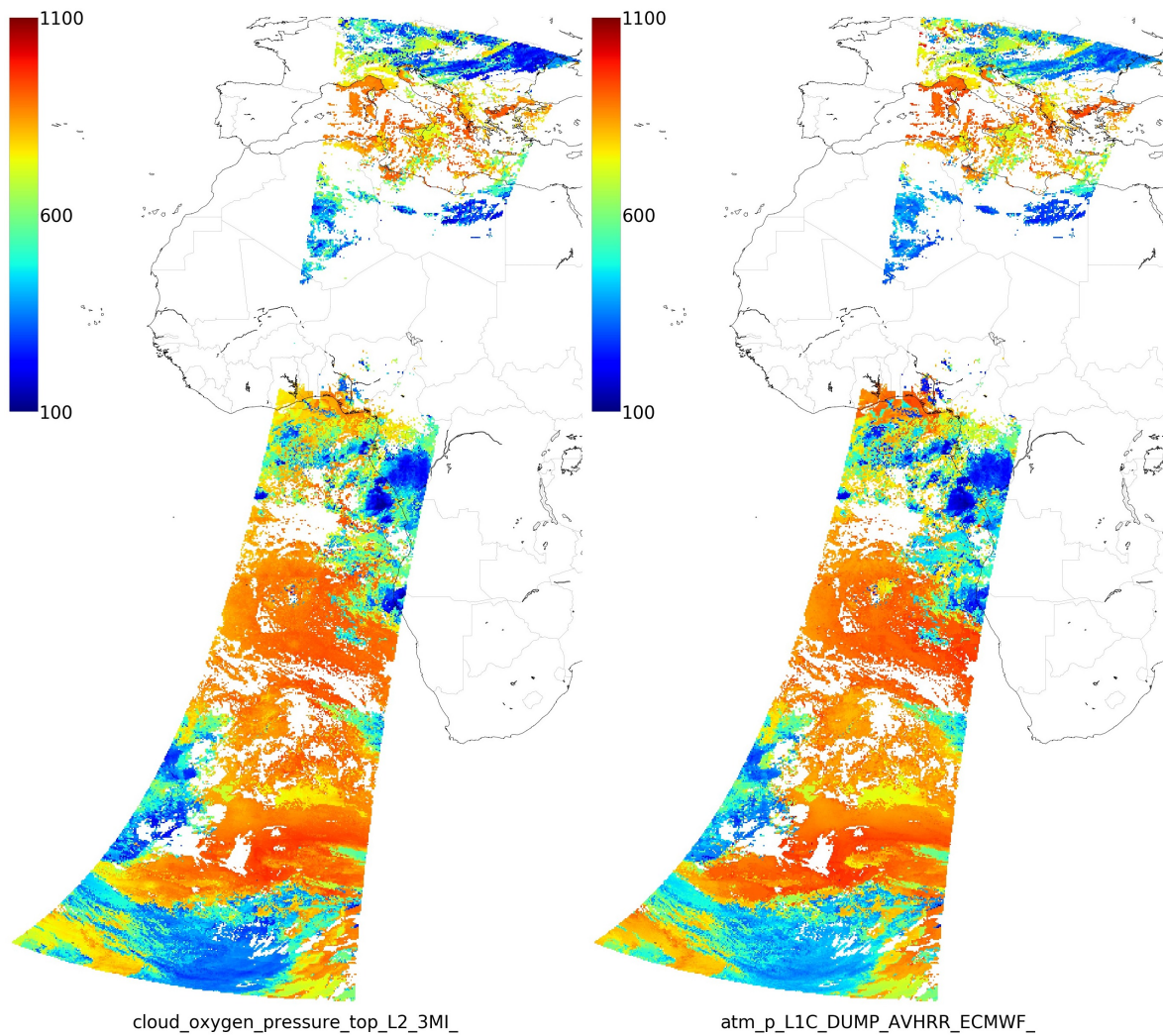


Figure 23 : Cloud top pressure retrieved from O2-A band algorithm (CLOVES output – top left) against estimated cloud top pressure from ECMWF inputs (top right) along with global comparison scatterplot (bottom left).

6.4.2 Comparison by cloud phase

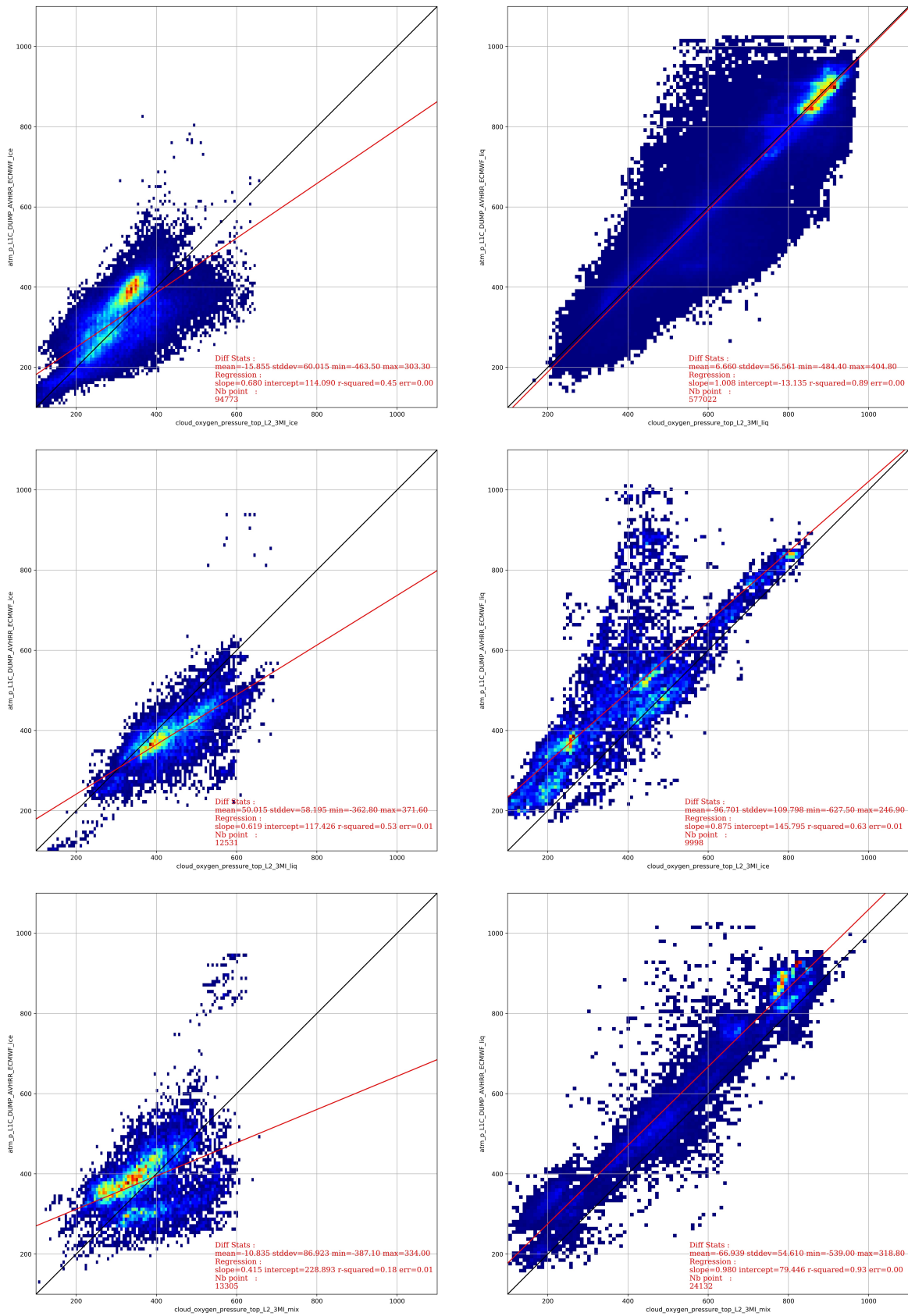


Figure 24 : Comparison between O2-A band retrieved and assumed cloud top pressure for different categories of retrieved and assumed cloud phase.

## 6.4.3 Cloud Apparent pressure &amp; Cloud Middle Pressure from O2-A band

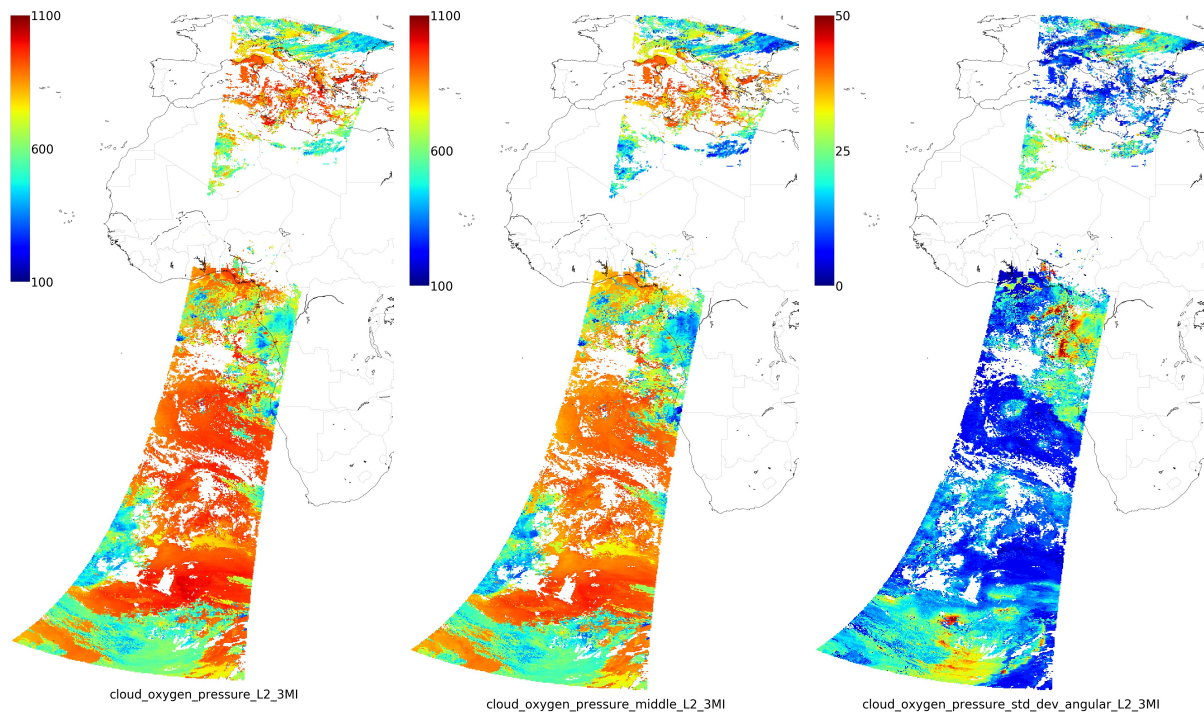


Figure 25 : Example of Cloud Apparent Pressure (derived from O2-A band – left), cloud middle pressures (CLOVES algorithm estimate) and standard deviation of the multiangle retrievals of Cloud Apparent Pressure.

6.5 Cloud Geometrical Thickness

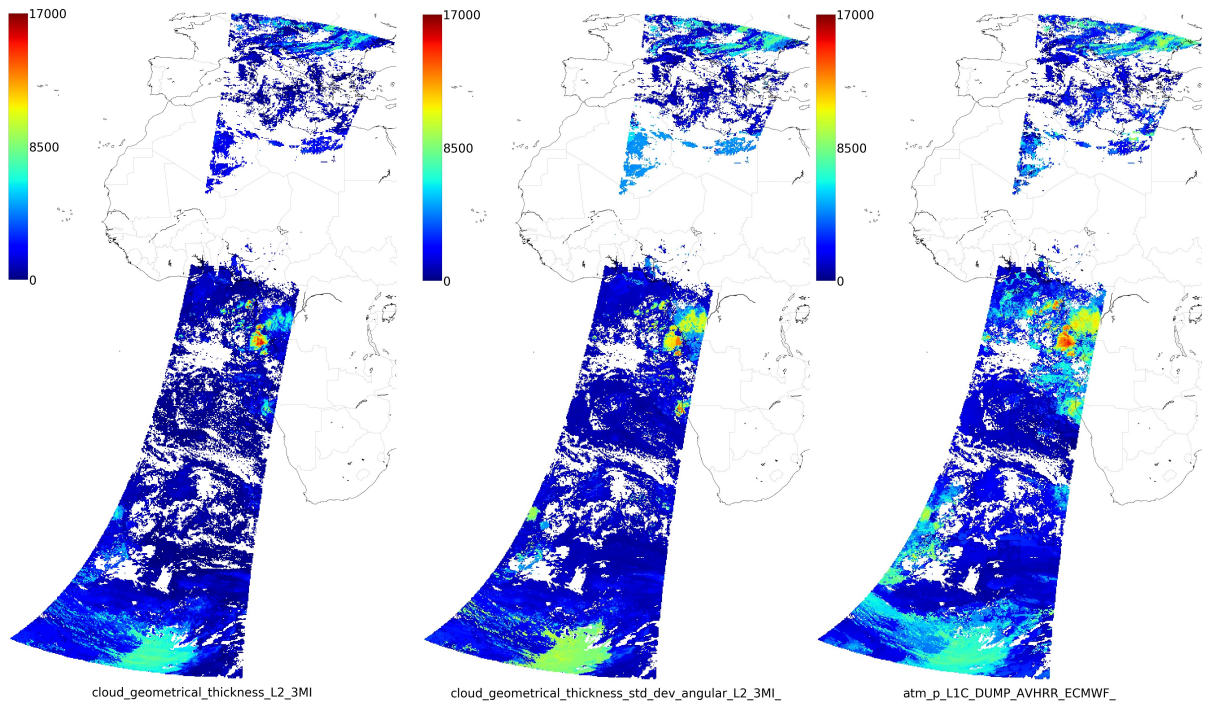


Figure 26: Cloud geometrical thickness retrieved from Cloud Top and Cloud Middle Pressure (left), Cloud Geometrical Thickness inferred from standard deviation of the multiangle O2-A band cloud apparent pressure retrievals (centre) and Geometrical Thickness assumed for test data simulation from ECMWF.

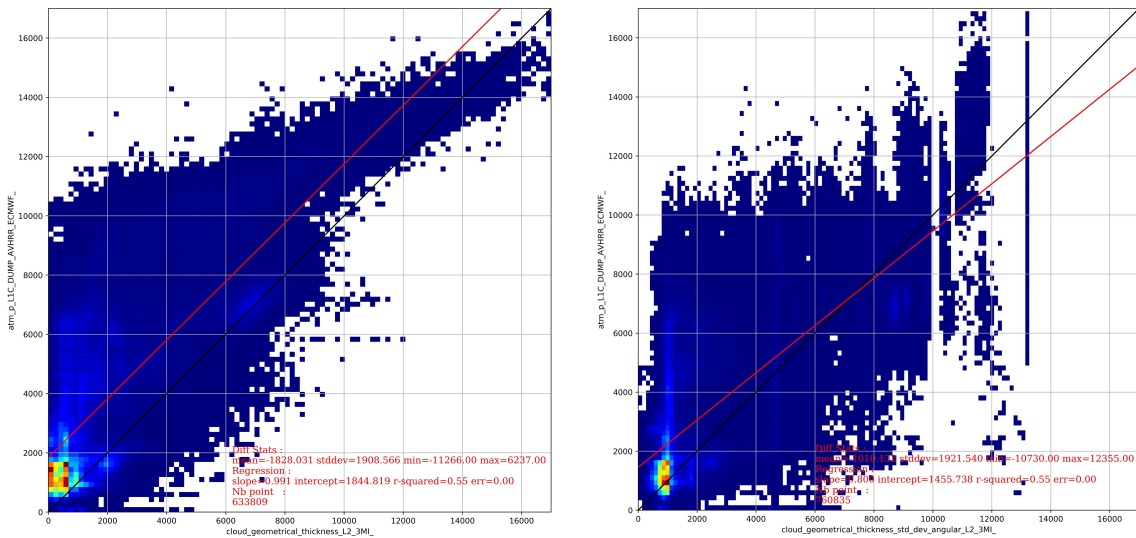


Figure 27: Comparison between Cloud Geometrical Thickness(CGT) inferred from differences between CTOP and CMOP (left) and CGT derived from multiangle standard deviation of PAPP.

## 6.6 Multilayered Clouds Occurrence

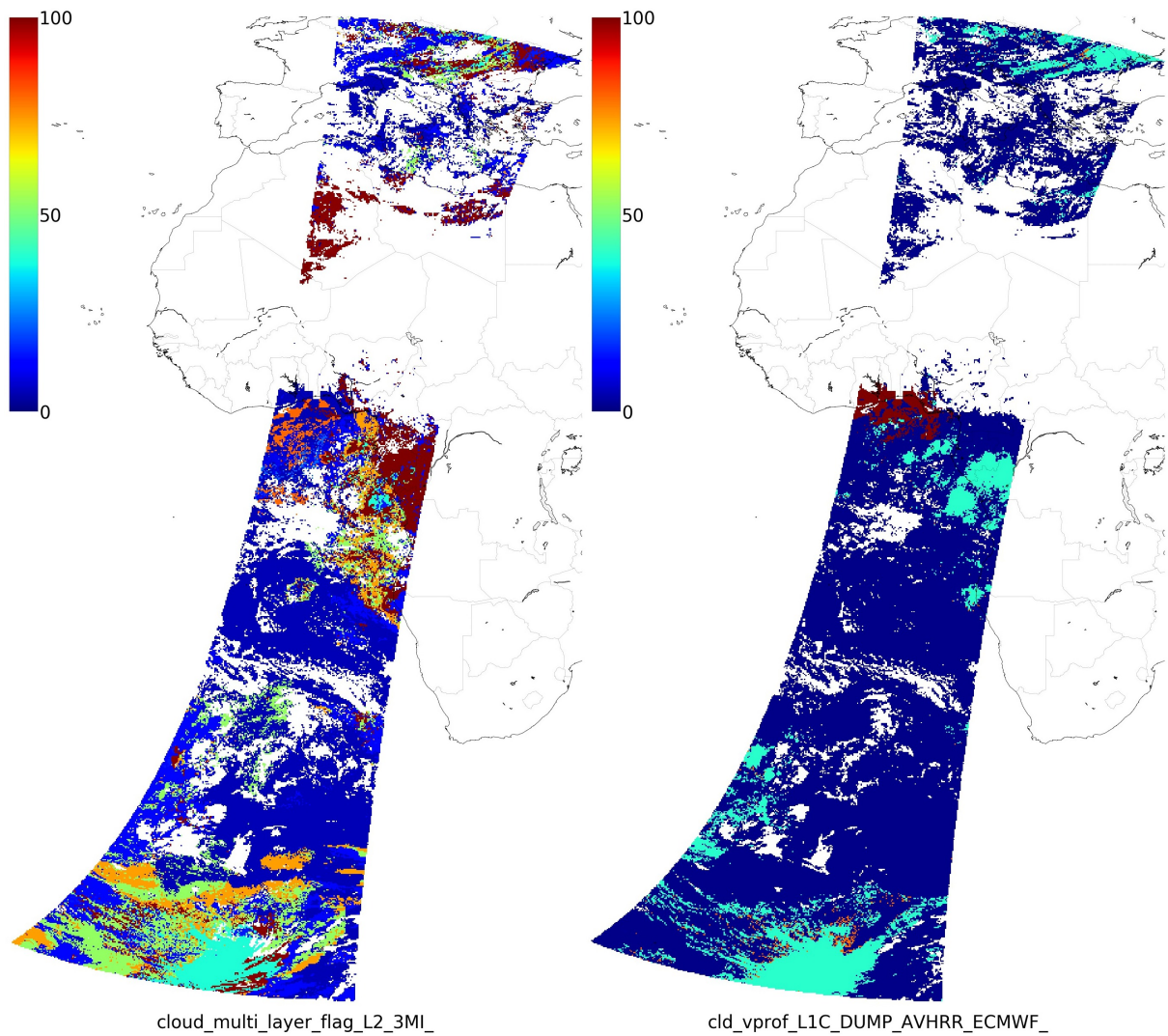


Figure 28: Example of multilayer flag output from the multi-layered cloud detection algorithm. Here for TDS V4, the probability of multilayer situations exhibit a large range due to the extended and variable ECMWF cloud profiles used for simulation.

### 6.7 Cloud Optical Thickness

#### 6.7.1 Global Comparison

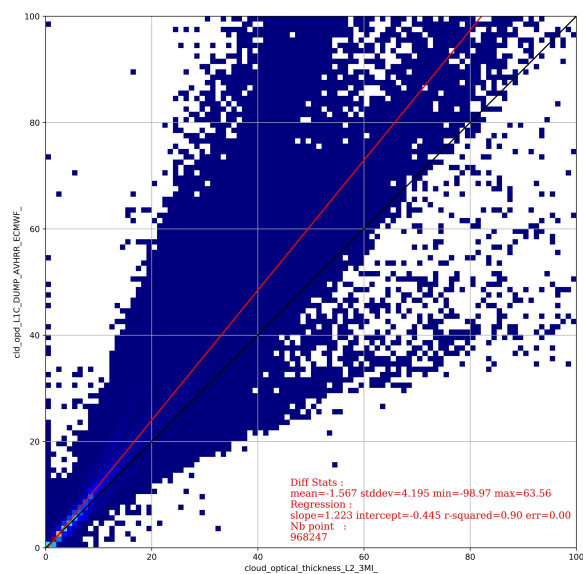
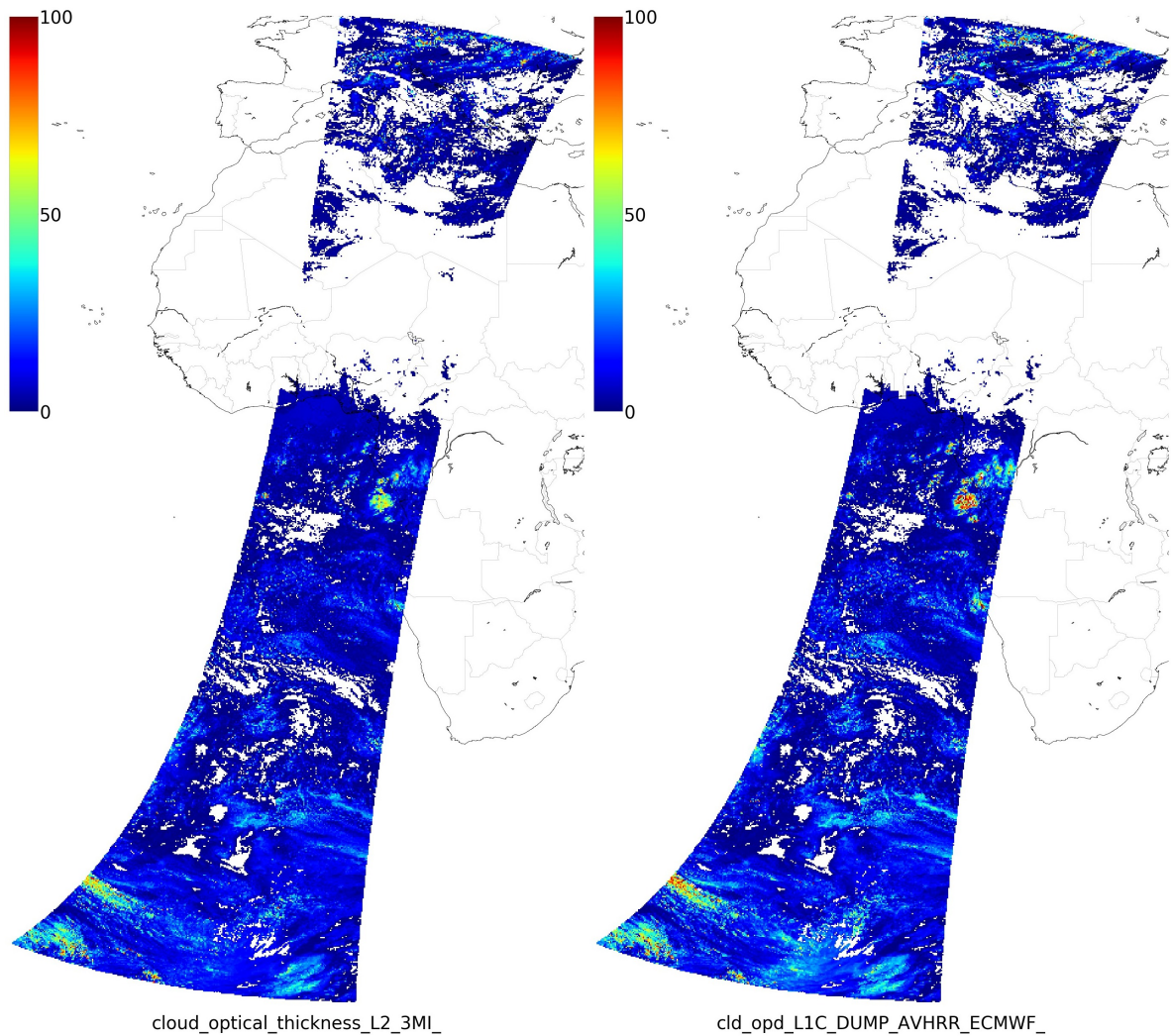


Figure 29 : Example of cloud optical thickness retrieved (top left) against assumed cloud optical thickness from a combination of AVHRR products and ECMWF profiles (top right). A global scatterplot (left) shows the general good agreement between assumed and retrieved cloud optical thickness as well as outliers caused by erroneous phase detection.

6.7.2 Comparison by cloud phase

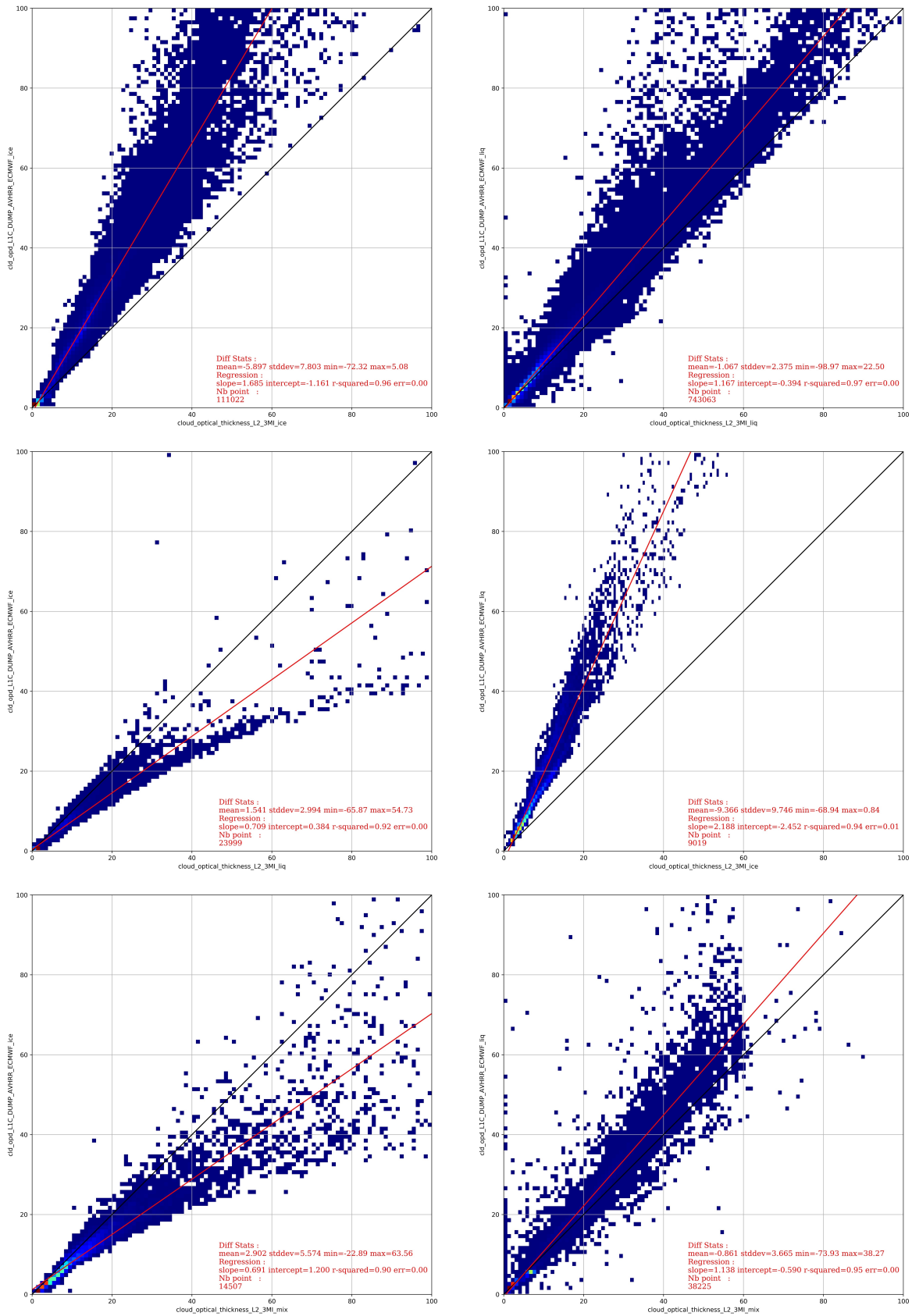


Figure 30 : Scatterplots of assumed against retrieved cloud optical thickness for different combinations of assumed/retrieved cloud top phase. Correlation between retrieved and assumed optical thickness is very good for liquid clouds but erroneous phase assumptions and multilayer situations (ice over liquid detected as ice only) lead to systematic biases in cloud optical thickness retrievals.

6.8 Cloud Particle Effective Radius

6.8.1 Global Comparison

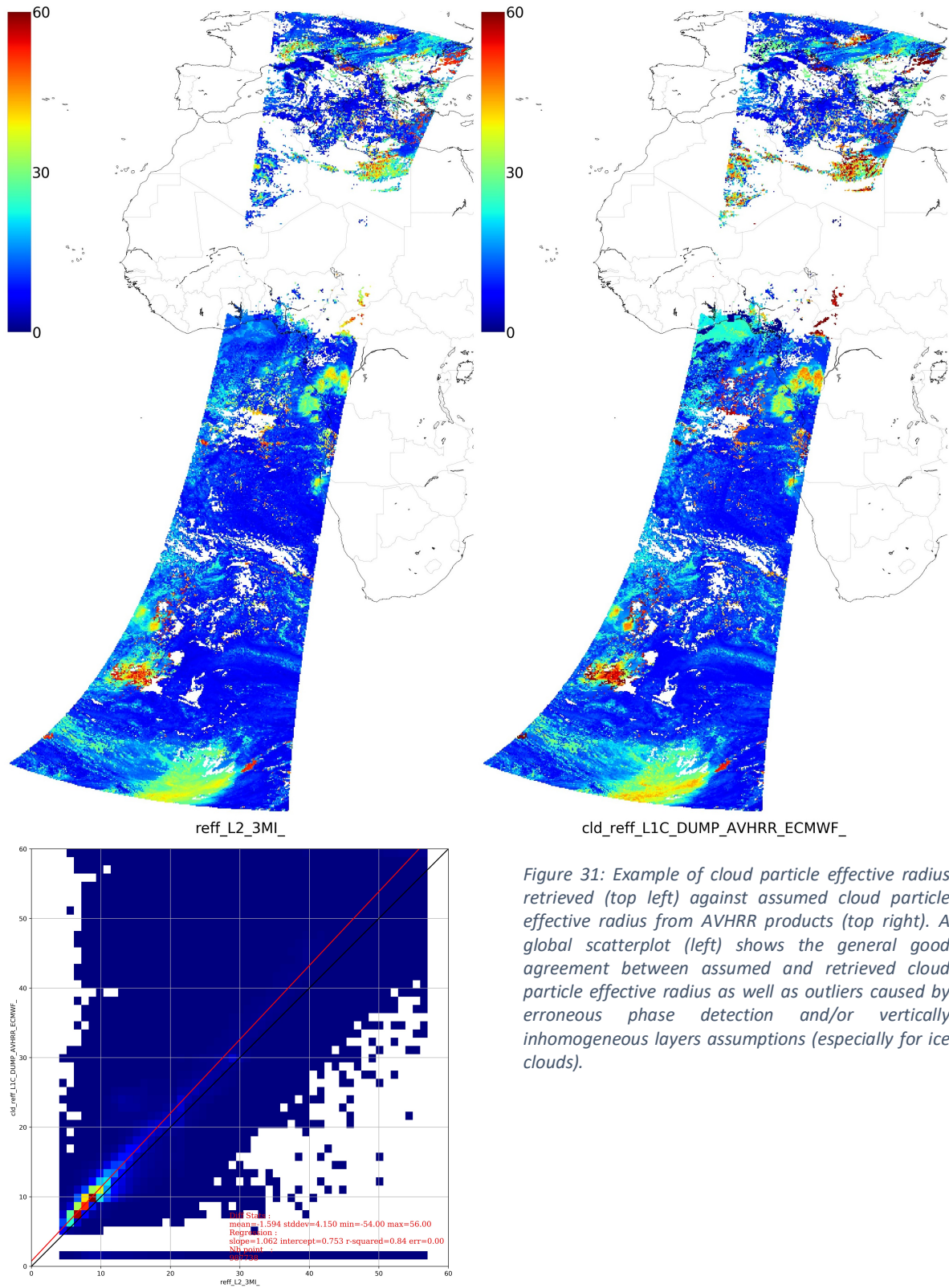


Figure 31: Example of cloud particle effective radius retrieved (top left) against assumed cloud particle effective radius from AVHRR products (top right). A global scatterplot (left) shows the general good agreement between assumed and retrieved cloud particle effective radius as well as outliers caused by erroneous phase detection and/or vertically inhomogeneous layers assumptions (especially for ice clouds).

6.8.2 Comparison by cloud phase

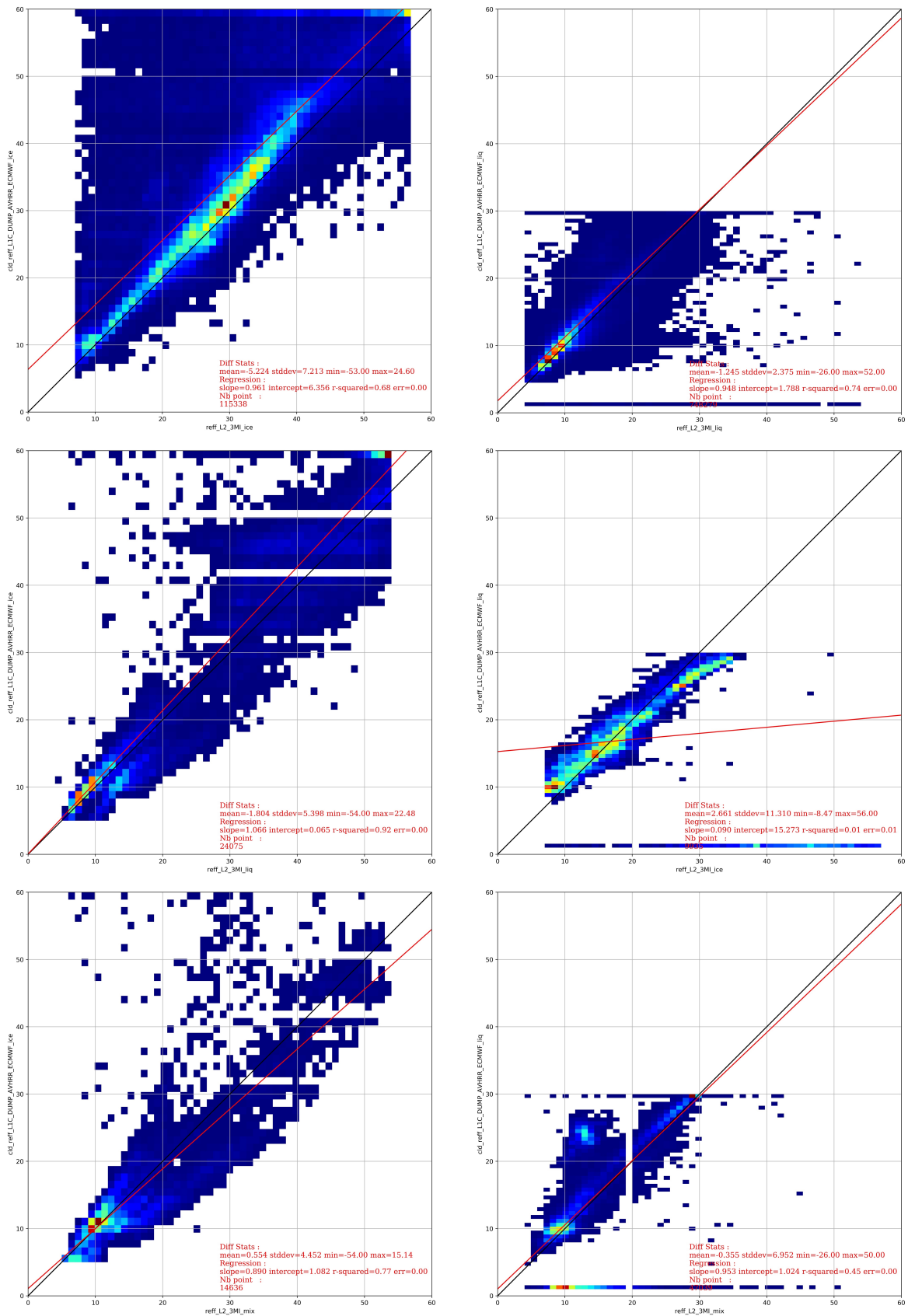


Figure 32: Comparison between assumed and retrieved cloud particle effective radius for different combination of retrieved/assumed cloud phase. Agreement is generally good when cloud phase detection agrees with assumed optical properties used for test data simulation.

## 6.9 Cloud Spherical Albedo &amp; Shortwave Albedo

## 6.9.1 Examples

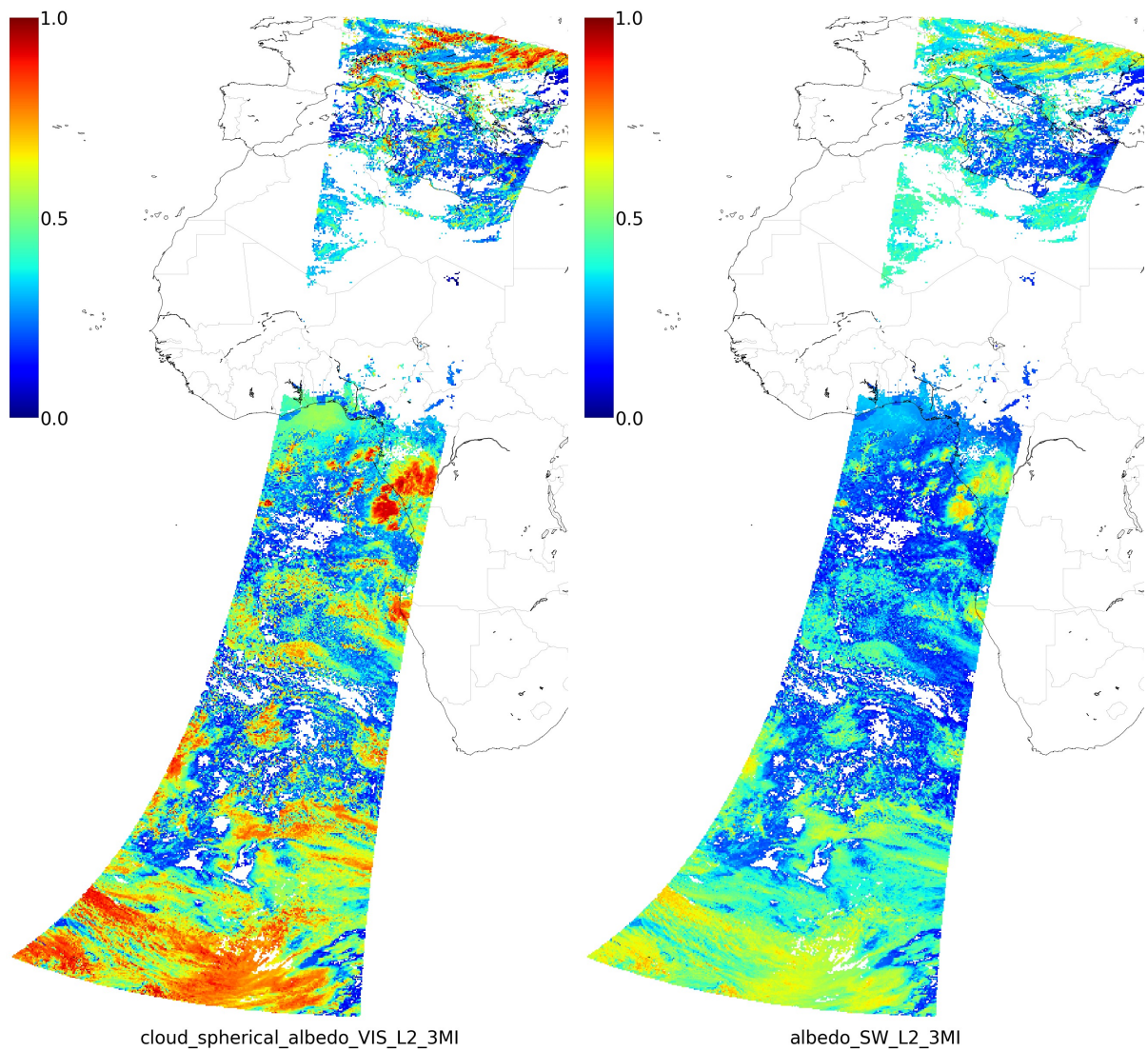


Figure 33: Example of Cloud Spherical Albedo and integrated Shortwave Albedo products retrieved from Test Data Set V4.0.

## 7 Discussion of results and accuracy evaluation

### 7.1 Expression of requirements

It should first be noted that the product evaluation performed during this study is limited in terms of statistical representativeness due to the limited amount of test data available. However, the main advantage of the approach applied here (application to realistic test data as opposed to purely theoretical sensitivity analysis) is that the demonstrated performances account for the actual observation geometries of 3MI and the variable information content of 3MI observation for different parts of the orbit and swath.

In order to discuss the currently demonstrated product accuracy and conclude on the expected performance, we are reminding here the observational requirements currently expressed by WMO and GCOS for the cloud variables that are directly or indirectly observable by the 3MI and retrieved using the prototype software.

Most uncertainties are expressed in meaningful units except maybe for the cloud type product for which accuracy is expressed as inverse of number of classes, so that smaller figures correspond to better performance. For a Cloud Phase algorithm detecting ice, liquid or mixed types (3 classes) the target (resp. threshold) uncertainty is for example 0.1 (resp. 0.2) Classes<sup>-1</sup> which, if our understanding is correct, translates to ~3,3% to 6.6% of false identification.

Numbers provided in Table 6 and Table 7 are to be compared with currently expressed requirement for the VII cloud products (Table 5), bearing in mind that VII is the primary instrument for cloud observation on EPS-SG and that 3MI is primarily designed for aerosol observations.

Parameter	Horizontal resolution	Accuracy (goal)
Cloud detection (*)	Pixel (500m)	5%
Cloud Top Pressure	Cloudy pixel	50 hPa
Cloud top phase (*)	Cloudy pixel	10%
Cloud Optical Thickness (*)	Cloudy pixel	50%
Cloud Particle Effective Radius (*)	Cloudy pixel	5 μm
Liquid/ice water path	Cloudy pixel	50%
Water vapour total column	Clear pixel (Objective: 1km)	5%

Table 5 : Summary of VII cloud products accuracy (goal) requirements. (\*) indicates requirements is also applicable to 3MI based on Mission Requirements.

Variable	Application Area	Layer(s)	Uncertainty			
			Goal	Breakthrough	Threshold	
Cloud cover	Global NWP	TC	5	10	20	%
Cloud cover	High Res NWP	TrC	5	8	20	%
Cloud cover	Nowcasting / VSRF	TrC	5	10	20	%
Cloud type	Nowcasting / VSRF	n/a (2D)	0,1	0,125	0,2	Classes <sup>-1</sup>
Cloud drop effective radius	Global NWP	Cloud-top	1	2	5	μm
Cloud drop effective radius	High Res NWP	Cloud-top	1	2	5	μm
Cloud drop effective radius	Climate Monitoring (GCOS)	Cloud-top	1			μm
Cloud ice Total Column	Global NWP	TC	5	10	20	g.m <sup>-2</sup>
Cloud ice Total Column	High Res NWP	TC	10	13	20	g.m <sup>-2</sup>
Cloud liquid water (CLW) total column	Global NWP	TC	10	20	50	g.m <sup>-2</sup>
Cloud liquid water (CLW) total column	High Res NWP	TC	10	20	50	g.m <sup>-2</sup>
Cloud optical depth	Climate Monitoring (GCOS)	TC				dimless
Cloud top temperature	Nowcasting / VSRF	Cloud-top	0,5	0,8	2	K
Cloud top temperature	Climate Monitoring (GCOS)	Cloud-top	1		5	K
Cloud base height	Global NWP	n/a (2D)	0,2	0,5	1	km
Cloud base height	High Res NWP	n/a (2D)	0,1	0,25	0,5	km
Cloud base height	Nowcasting / VSRF	n/a (2D)	0,1	0,25	0,5	km

Table 6 : Cloud observation requirements expressed as Goal, Breakthrough and Threshold for different applications (Global & High Resolution NWP, Nowcasting, Climate Monitoring (GCOS)) (From : <http://www.wmo-sat.info/oscar/requirements>).

### Target Requirements

Variable/ Parameter	Horizontal Resolution	Vertical Resolution	Temporal Resolution	Accuracy	Stability
CA	50km	N/A	3h	0.01 – 0.05	0.003 – 0.03
CTP	50km	N/A	3h	15hPa – 50hPa	3hPa – 15hPa
CTT	50km	N/A	3h	1K – 5K	0.2K – 1K
COD	50km	N/A	3h	10%	2%
CWP	50km	N/A	3h	25%	5%
CRE	50km	N/A	3h	5%–10%	1%–2%

Table 7 : Target requirements for clouds ECV as summarized by GCOS in terms of accuracy and stability

## 7.2 Results discussion

Following this reminder on target accuracy for the main products of interest we will now discuss the results presented in sections 5 and 6. While we have presented figures separately for TDS V3.2 and V4.1, we will discuss the results jointly for each product in order to stress out their main advantages and limitations.

Also, results and figures have been presented here only for one orbit, but similar results have been obtained for the two additional TDS V4.1 orbits that are part of the 3MI & VII synthetic observations test data.

### 7.2.1 Cloud Detection

Results for cloud detection are clearly within requirements with 3% of false detection in case of simplified physics and a surprisingly even better detection rate (2%) for TDS V4.1 although the difference is not significant. Main uncertainties in cloud detection are in line with well know caveats of such products. As can be seen from Figure 7 and Figure 20, separation of thin clouds against aerosols over bright surfaces (Saharan regions) remains a challenge for sensors that do not benefit from thermal infrared channels. On Figure 20 we can also observe a higher level of uncertain clear detection over northern Europe compared to Figure 7, probably due to mixing of aerosol and clouds within the same pixels.

### 7.2.2 Cloud Thermodynamic Phase

For TDS V3.2, the cloud phase retrieved generally match very well the assumed binary mask from AVHRR (Figure 8). The score of correct identification is 83% and the false detection rate (ice instead of liquid or reversed) is only 5%. The remaining 11% correspond to ambiguous situation where either ice (8%) or liquid (3%) clouds are retrieved as mixed/uncertain. Note here that mixed clouds will be treated as liquid phase for further retrieval of optical properties (COT, CER). The mixed/uncertain situation are detected primarily on edges of cloud systems when cloud optical thickness becomes small ( $< 1.0$ ), typically at the edges of deep convective cloud anvils or for cloud edges in broken cloud fields. Figure 21, shows a similar picture for the TDS V4.1 retrievals where we can however observe a much higher fraction of dominantly liquid phase clouds due to ECMWF IWC/LWC profiles assumption. Regardless, the correct identification rate is 87% in that case and erroneous detection are down to 4%, with 9% of clouds remaining uncertain.

When applied to the 3 test orbits, the statistics exhibit even better scores as shown by Figure 36 below. The main explanation for those differences is that one of the additional orbit corresponds mainly to ocean scenes where phase detection is less biased by bright surfaces. For performance evaluation we summarize the statistics obtained over the 3 test orbits of TDS V4.1. As can be seen from results summarized in Table 8, the cloud phase product meets the observation requirements and even exceeds the goal when mixed phase clouds are treated as liquid (as is applied by the optical properties retrieval algorithms).

SCORES			SCORES WHEN MIXED TREATED AS LIQUID	
AGREEMENT	ERROR	MIXED	AGREEMENT	ERROR
90%	3%	7%	95%	5%

Table 8: Statistics summary for cloud phase product expressed in terms of AGREEMENT and ERROR

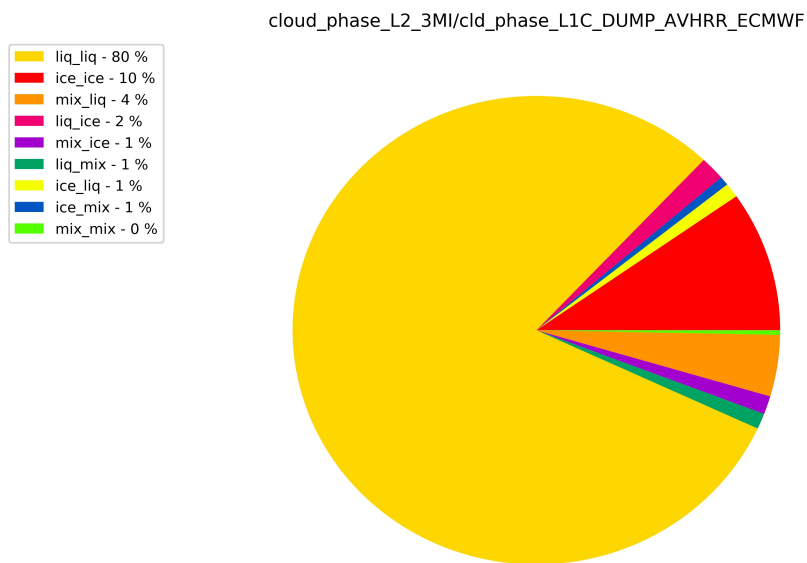


Figure 34: Statistics of detection agreement for the Cloud Phase product aggregated for the 3 available orbits of TDS V4.1

### 7.2.3 Cloud Top Pressure from Rayleigh (PRAY) and Scene Apparent Pressure (PAPP)

Examples of the cloud top pressure derived from polarization signal created by Rayleigh scattering (PRAY) and scene apparent pressure (PAPP) derived from O2-A band differential absorption are presented in Figure 9 and Figure 22 respectively for TDS V3.2 and V4.1.

These products have not been directly compared to cloud top height as this information is only produced to serve as input for other algorithms (cloud detection, cloud phase, multilayer situations including aerosol above cloud detection).

The PRAY product is here a good illustration of the variable information content of 3MI across the instrument swath. On the western central part of the orbit, the range of scattering angles accessible by 3MI do not allow to retrieve PRAY leading to missing information for those regions. Also, comparing PRAY and PAPP or PO2 (Figure 10 and Figure 23) stress out the clearly different sensitivity of those methods to cloud top height due to the different weighting functions of spectral channels and polarization/total radiance signal.

### 7.2.4 Cloud Top Pressure from O2-A band (CTOP)

On Figure 10 and Figure 23, we compare the Cloud Top Pressure (CTOP) derived from O2-A band differential absorption signal to the cloud top pressure specified for TDS simulation.

Global comparison shows the good correlation of retrieved product with assumed cloud top pressure with no obvious issues appearing from the geographical distributions.

Further analysis can be made by looking at correlation between retrieved and assumed CTOP for different categories defined by cloud phase (Figure 11 and Figure 24). For both TDS V3.2 and V4.1, the observed correlation are particularly good for all liquid clouds whereas ice clouds having higher vertical extension tend to present larger biases. The largest differences are observed for ice clouds over bright surfaces (Sahara) as will be explained later on by looking at cloud apparent pressure and its angular variability.

The global statistics are summarized in Table 9 demonstrating that the CTOP product is in line with expressed requirements. It is interesting to note that the algorithm seems to perform better on TDS V4.1 which have much more complex cloud vertical structure. This

counterintuitive result is in fact associated to the fact that coefficients used by the CLOVES algorithm have been optimized on real cloud profiles observed by CLOUDSAT/CALIPSO. Therefore, correction factors are better suited for clouds having realistic geometrical extension than for homogenous cloud layers specified in TDS V3.2.

TDS Version	Slope	Intercept	r-squared
V3.2	0.90	78	0.96
V4.1	0.96	27.6	0.92

Table 9: Summary statistics for linear correlation between retrieved and assumed cloud top pressure.

### 7.2.5 Cloud Apparent pressure & Cloud Middle Pressure from O2-A band

Cloud apparent pressure is derived by interpreting the total absorption pathlength occurring in two 3MI channels centered on the O2-A band. For a perfect reflector, the apparent pressure would correspond to cloud top but multiple scattering occurring inside clouds increase the actual photons pathlength, leading to an apparent pressure at a level within the cloud. The exact level actually depends on cloud geometrical thickness and cloud extinction profile, so that multiangle retrievals of cloud apparent pressure exhibit a stronger angular variation when clouds get optically and geometrically thicker. The CLOVES algorithm (Ferlay et al, 2010) provides an estimate of cloud middle pressure by applying correction factors to PAPP depending on COT. Figure 12 and Figure 25 present the initial cloud apparent pressure and the corrected Cloud Middle Pressure along with the standard deviation of the multiangle PAPP retrievals. For TDS V3.2, the PAPP angular standard deviation is fairly small since clouds are assumed to be homogeneous with almost fixed and small geometrical thickness. At the opposite TD V4.1 do exhibit much stronger angular standard deviation of PAPP due to cloud profiles extending over deeper layers.

We are not discussing here the PAPP and CMOP product in details and rather focus on the Cloud Geometrical Thickness product hereafter.

### 7.2.6 Cloud Geometrical Thickness

Cloud Geometrical Thickness (CGT) is inferred by the CLOVES algorithm by two techniques. The first one (CGT\_D) is simply deduced by differentiating the Cloud Top and Cloud Middle altitude (obtained from CTOP and CMOP), and the second technique (CGT) uses a statistical relation linking angular variability of PAPP to Cloud Geometrical Thickness. Coefficients of the statistical relation have been established by comparing the observed variability of PAPP from POLDER observation to CGT determined directly by active sensors (CLOUDSAT/CALIPSO). Therefore, the CGT product is expected to provide reasonable information only when realistic cloud profiles are considered and we will here focus on the results obtained for TDS V4.1. Results from TDS V3.2 are presented in Figure 13 for illustration only.

Results for TDS V4.1 are presented in Figure 26 and scatterplots for comparison against input parameters are shown in Figure 27. It appears from those figures that CGT retrievals are moderately correlated with actual cloud thickness set in simulation, with r-squared coefficient of 0.55 for both products and slopes for linear regression of 0.99 and 0.80 respectively from CGT\_D and CGT. Note however that the products are designed to work on single layer clouds and that coefficients of statistical parametrization have been optimized for POLDER channels from actual observation. The simulated TDS V4.1, even though it introduced cloud vertical variability, might not be fully representative of real clouds in terms of vertical extinction

profiles. Future work could include the development of new parameterization developed specifically for 3MI from purely theoretical learning database.

#### 7.2.7 Multilayered Clouds Occurrence

The Multi-Layers Flag product (MLF) provides a detection of potentially multilayered situation by mean of a probability index. The higher the index, the more likely a multilayered cloud system is being observed.

In TDS V3.2, all clouds were simulated as single layers and the retrieve product (Figure 14) clearly exhibit very low probability of multilayered situations.

Results for TDS V4.1 are illustrated in Figure 28, showing a much more diverse range of MLF values. The use of ECMWF cloud profiles did not allow for simulation of very well separated cloud layers and the index derived from ECMWF (right image in Figure 28) mainly indicates very extended cloud systems with well separated liquid and ice layers. We can note however that the MLF index identifies high probability for the Southern Atlantic Ocean frontal system area as well as the outflows of the convective system in the central part of the orbit.

Further validation of this product is not possible from the current test data set but the logic and performance of the algorithm has been validated from POLDER observations using CLOUDSAT/CALIPSO (Desmons et al, 2013). The modular nature of the decision tree can be easily modified to incorporate additional information at a later stage, for instance to use the 3MI 1.37 micrometer channels or infrared bands of the VII in a synergistic algorithm.

#### 7.2.8 Cloud Optical Thickness

Cloud Optical Thickness (COT) product is illustrated on Figure 15 and Figure 29, and detailed comparison by cloud phase are presented in Figure 16 and Figure 30.

Retrieval of COT (as well as CER) is highly dependent on cloud microphysical assumptions (optical properties) and to a lesser extent to the vertical structure of clouds.

In our proposed implementation (as in almost any operational retrieval algorithm), COT is retrieved under the assumption that cloud is composed of particles either in ice or liquid phase. Evaluation of the algorithm performance can therefore strictly be made only through TDS V3.2 where clouds are assumed to be single layers and single phase.

For TDS V3.2, Figure 15 and Figure 16 demonstrate that the implementation of COT algorithm is perfectly valid and retrieved values are in extremely good agreement with input parameters, with correlation coefficients of 0.99 for both liquid and ice cloud retrievals (when phase is consistent between assumed and retrieved parameter). Linear regression slopes are 1.06 and 1.02 for ice and liquid cloud respectively. Naturally, much larger systematic biases appear when COT is retrieved using the wrong phase assumption as has been extensively discussed by Zeng et al (2012). Overall however, the cloud phase identification mismatch has a limited impact on global statistics, and correlation coefficient remains high at 0.96, with a linear slope of 1.03 all clouds being considered.

Results for TDS V4.1 (Figure 29 and Figure 30) demonstrates similarly very good performances for liquid clouds but a significant bias appears for clouds detected as ice. The reason behind this is that a vast majority of ice topped clouds also contain a significant fraction of liquid phase water content in the lower part as specified by ECMWF profile. Since COT retrieval uses an ice optical properties model for an actually mixed phase cloud, the retrieval is systematically biased low because the liquid part of the cloud is not correctly accounted for. This effect might be exaggerated by the ECMWF profiles that tend to contain too much liquid water content

compared to real clouds, but it stresses out the critical importance of accounting for the vertical structure of a cloud when attempting properties retrieval.

From these results we can conclude that the algorithm implementation is valid and produce meaningful results but future work would be needed to handle mixed phase cloud situation. Synergistic use of different EPS-SG sensors could open perspectives towards that objective.

#### 7.2.9 Cloud Particle Effective Radius

As for the COT product, Cloud Effective Radius (CER) retrieval are highly dependent on cloud model assumptions in terms of optical properties and their vertical variability.

The results obtained for TDS V3.2 ( Figure 17 and Figure 18) clearly demonstrate that the implemented algorithm allows to retrieve CER with very good accuracy as long as the cloud phase is correctly identified. The apparent “asymptotic” behavior around 32 microns observed for liquid clouds is a side effect of the CER variation introduced in TDS 3.2 to mimic spectrally dependent SWIR channels penetration depth combined with the rather small cloud geometrical thickness assumption. This behavior disappears when vertical profile of CER is explicitly introduced as can be seen from the same plot on Figure 32 or Figure 6 previously discussed.

Results obtained for TDS V4.1 are presented in Figure 31 and Figure 32. They demonstrate the good behavior of the retrieval algorithm even in those complex situations where CER is varied vertically and assumptions need to be made to convert the vertical profile of CER into a unique number for comparison. Again, a next step for this product would be to further develop an algorithm that would explicitly account for the vertical variation of CER and cloud extinction coefficient.

#### 7.2.10 Cloud Spherical Albedo & Shortwave Albedo

The Cloud Spherical Albedo (ASVIS) and Shortwave Albedo (ASW) products are illustrated in Figure 19 and Figure 33. Those products are derived directly from other parameters describing cloud cover (COT, CER) and the Look-Up tables use for their retrieval. Since ASVIS and ASW are not explicitly set in simulation (they derive from specified COT and CER), there is no real interest in comparing the retrieved value to the assumed one. Illustrations are only provided here to demonstrate the implementation status of the two products.

## 8 Conclusions and perspectives

### 8.1 Conclusions

From the discussion of results presented in section 7, we conclude that the Day-1 algorithms implemented and tested through the present study allow to retrieve products with accuracies that meets or exceed the 3MI mission goal requirements for clouds.

The proposed algorithms have been tested on synthetic test data containing realistic diversity of situations (cloudy and clear sky observations) that are perfectly representative of the 3MI future observations in terms of angular sampling. The delivered prototype software has been demonstrated to be fully compliant with NRT requirements based on even limited computational resources.

## 8.2 Expected potential improvements

### 8.2.1 Cloud effective radius from polarization

Although it was not discussed in the present report, an implementation of liquid cloud effective radius and effective variance retrieval using multiangle multispectral (visible/near-infrared only) polarization observation has been implemented and delivered in the prototype software. This algorithm can be easily extended to use the new 3MI SWIR channels and provide a consolidated estimate for CER and effective variance of droplet size distribution at cloud top.

### 8.2.2 Uncertainties estimates

Several of the products developed and presented here could benefit from an explicit calculation of associated uncertainties by propagating radiometric uncertainties and some model assumptions through the LUT based retrievals. Also, several quality flag could be formalized for cloud detection and cloud phase based on individual tests applied internally to the algorithm. Generally speaking, the entire set of products delivered here could be completed by uncertainties which need to be formalized and can be a logical topic for future developments.

### 8.2.3 Cloud ShortWave albedo

The current implementation of the integrated shortwave albedo only uses 3 visible and near infrared channels following the historical POLDER implementation. With the increased 3MI spectral range, the algorithm and product would benefit from incorporating SWIR channels for the conversion of spectral narrow band cloud albedo to full integrated cloud shortwave albedo.

### 8.2.4 Vertical variability of cloud properties

As was clearly illustrated by the discussion of results in section 7, the cloud properties retrieved under the assumption of homogeneous, single phase cloud layer exhibit residual systematic biases that can only be overcome by considering explicitly the vertical variation of cloud properties. Therefore, a logical next step for improvement of 3MI cloud products would be to implement an algorithm able to handle consistently all 3MI observations in order to optimize a representation of cloudy column allowing for vertical variation of cloud phase, cloud extinction and cloud particle effective radius (or any combination of related parameters such as IWC/LWC, ...).

Initial studies (Merlin et al, 2015; G. Merlin PhD) have demonstrated that 3MI observations information content could actually be sufficient to constrain the retrieval of a cloud vertical profile constrained to a simple shape. Under the assumption that the cloud extinction profile can be described by a simple triangle shape specified by its vertical location, extent and a simple parameter describing the position of the maximum IWC or LWC, we have implemented a prototype algorithm that uses 3MI observations in an optimal estimation framework to simultaneously retrieve CTOP, CGT and the vertical profile of CER and extinction coefficient. An example of such a retrieval is shown in Figure 35. The retrieval is initialized here with a first guess (orange profile) using the COT, CTOP and CGT retrieved from the operational algorithm and parameters are optimized using an optimal estimation approach to obtain a better

description of cloud vertical variability (green profile) that could be more representative of the actual profile (blue curve) while being fully consistent with the 3MI multi-spectral, multi-polarization, multi-angle observations.

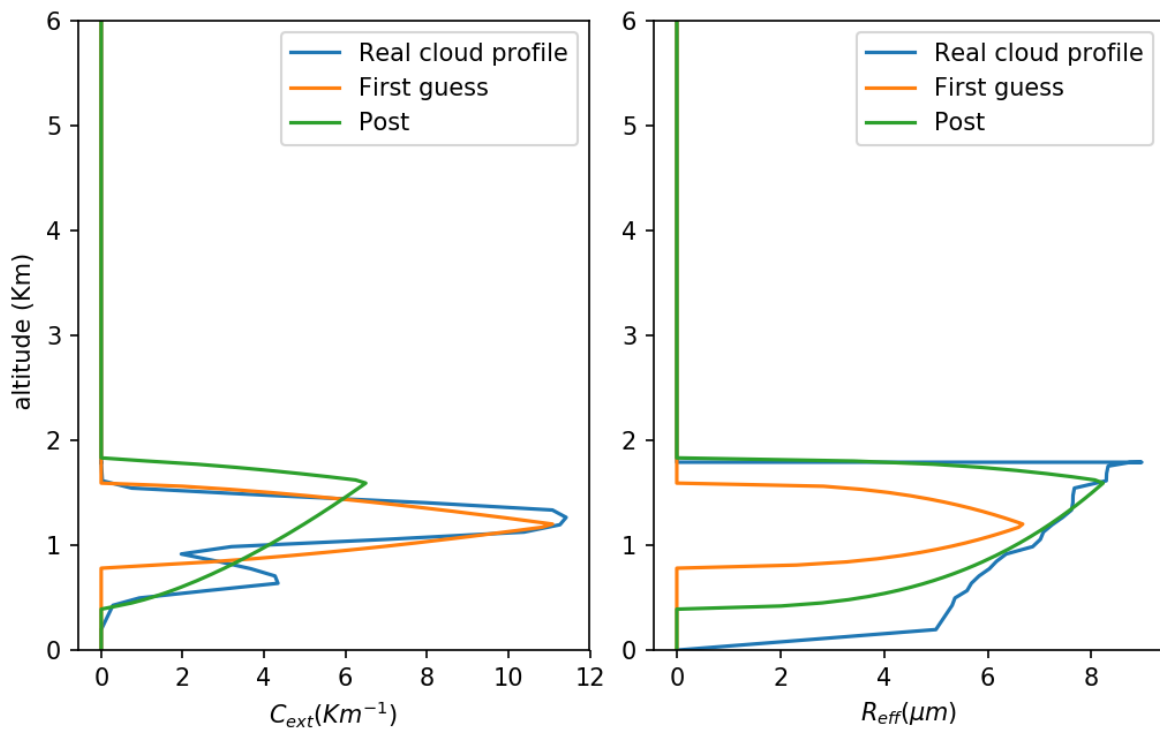


Figure 35: Example of retrieval of a cloud extinction and effective radius vertical profile using 3MI channels in an optimal estimation retrieval framework.

Such an approach is obviously extremely computationally expensive and intermediate steps could be implemented to retrieve only CTOP, CGT and COT in a first step. This approach has been tested already on POLDER data and compared to CloudSat/Calipso observations showing promising results. It would already represent a significant advance for the retrieval of CGT compared to the actual statistical approach implemented which has clear limitations.

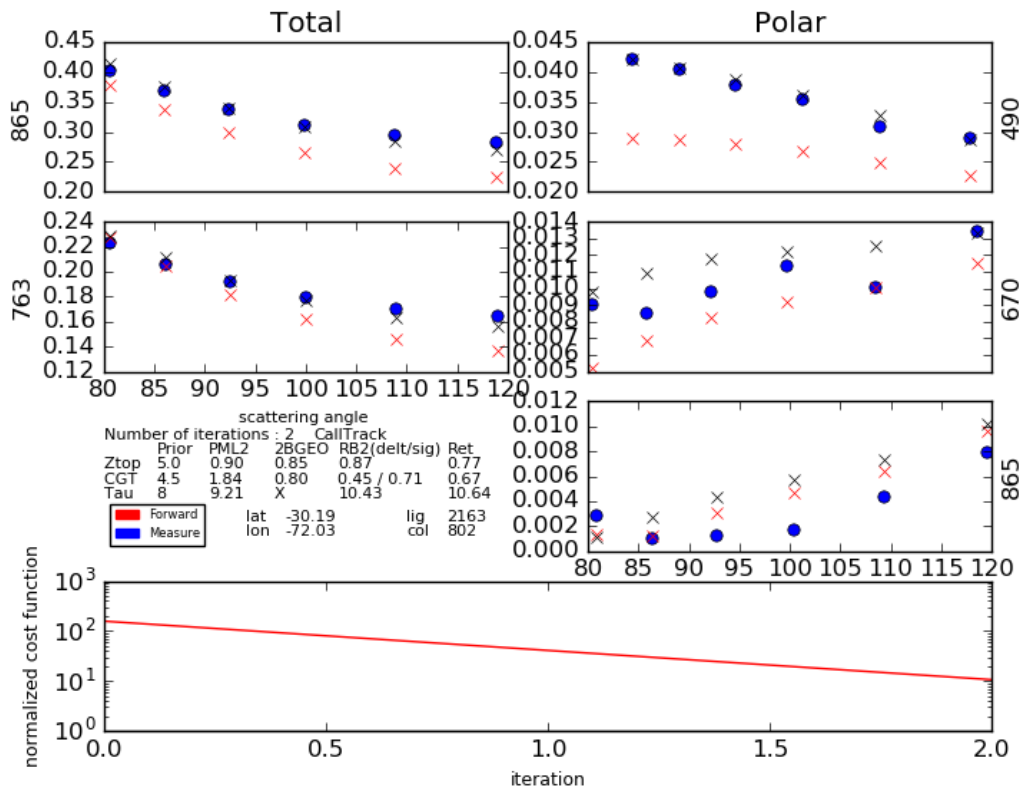


Figure 36: Example of validation of Ztop, CGT and COT retrievals obtained from the enhanced cloud vertical extent retrieval algorithm. Retrievals are compared to analog operational products from POLDER, MODIS and/or CLOUDSAT/CALIPSO.

## 9 References

- [1] Baran, A.J., Labonnote, L.C. On the reflection and polarisation properties of ice cloud (2006) *Journal of Quantitative Spectroscopy and Radiative Transfer*, 100 (1-3), pp. 41-54.
- [2] Baran, Anthony. J. and Labonnote, L.-C. (2007), A self-consistent scattering model for cirrus. I: The solar region. *Q.J.R. Meteorol. Soc.*, 133: 1899–1912. doi:10.1002/qj.164
- [3] Buriez, J-C; Parol, F; Poussi, Z; Viollier, M, An improved derivation of the top-of-atmosphere albedo from POLDER/ADEOS-2: 2. Broadband albedo, 2007, *JGRD*, 11219201
- [4] Buriez, J-C; Parol, F; Cornet, C; Doutriaux-Boucher, M, An improved derivation of the top-of-atmosphere albedo from POLDER/ADEOS-2: Narrowband albedos, 2005, *JGRD*, 110.5202
- [5] B. H. Cole, P. Yang, B. A. Baum, J. Riedi, and L. C.-Labonnote, Ice particle habit and surface roughness derived from PARASOL polarization measurements, *Atmos. Chem. Phys.*, 14, 3739-3750, doi:10.5194/acp-14-3739-2014, 2014
- [6] C. Cornet, C-Labonnote L., and F. Szczap, 2010, Three-dimensional polarized Monte Carlo atmospheric radiative transfer model (3DMCPOL): 3D effects on polarized visible reflectances of a cirrus cloud, *J. Quant. Spect. Rad. Transfer*, 111, 174-186, doi: 10.1016/j.jqsrt.2009.06.013.
- [7] Cox & Munk, Measurement of the roughness of the sea surface from photographs of the sun's glitter, *Journal of the Optical Society of America*, 1954, 44, 838
- [8] Desmons, M., Ferlay, N., Parol, F., Mcharek, L., and Vanbauce, C.: Improved information about the vertical location and extent of monolayer clouds from POLDER3 measurements in the oxygen A-band, *Atmos. Meas. Tech.*, 6, 2221-2238, doi:10.5194/amt-6-2221-2013, 2013.
- [9] Desmons M., N. Ferlay, F. Parol, J. Riedi, F. Thieuleux, 2016: A global multilayer cloud identification with POLDER/PARASOL, *J. Appl. Clim. Meteorol.*, vol. 56, 1121-1138.
- [10] Ferlay, N., F. Thieuleux, C. Cornet, A. B. Davis, P. Dubuisson, F. Ducos, F. Parol, J. Riédi, C. Vanbauce, 2010 : Toward new inferences about cloud structures from multidirectional measurements in the oxygen A band: Middle-of-cloud pressure and cloud geometrical thickness from POLDER3/PARASOL, *J. Appl. Meteor. Clim.*, doi: 10.1175/2010JAMC2550.1
- [11] King, N. J., and G. Vaughan (2012), Using passive remote sensing to retrieve the vertical variation of cloud droplet size in marine stratocumulus: An assessment of information content and the potential for improved retrievals from hyperspectral measurements, *J. Geophys. Res.*, 117, D15206
- [12] Kokhanovsky, A. and Rozanov, V. V.: Droplet vertical sizing in warm clouds using passive optical measurements from a satellite, *Atmos. Meas. Tech.*, 5, 517-528, doi:10.5194/amt-5-517-2012, 2012.
- [13] C.-Labonnote, L., Brogniez, G., Buriez, J.-C., Doutriaux-Boucher, M., Gayet, J.-F., Macke, A. Polarized light scattering by inhomogeneous hexagonal monocrystals: Validation with ADEOS-POLDER measurements (2001) *Journal of Geophysical Research Atmospheres*, 106 (D11), art. no. 2000JD900642, pp. 12139-12153.
- [14] H. Letu, H. Ishimoto, J. Riedi, T. Y. Nakajima, L. C.-Labonnote, A. J. Baran, T. M. Nagao, and M. Skiguchi, Investigation of ice particle habits to be used for ice cloud remote sensing for the GCOM-C satellite mission, *Atmos. Chem. Phys. Discuss.*, 15, 31665-31703, doi:10.5194/acpd-15-31665-2015, 2015 - Revised manuscript accepted for ACP

- [15] Maignan F., Bréon F.-M. and Lacaze R.: Bidirectional reflectance of Earth targets: Evaluation of analytical models using a large set of spaceborne measurements with emphasis on the Hot Spot, *Remote Sensing of Environment*, 90, 210–220, 2004.
- [16] Maignan, F., Bréon, F.M., Fédèle, E., and Bouvier M.: Polarized reflectances of natural surfaces: Spaceborne measurements and analytical modeling, *Remote Sensing of Environment*, doi:10.1016/j.rse.2009.07.022, 2009.
- [17] Merlin, G., Riedi, J., Labonnote, L. C., Cornet, C., Davis, A. B., Dubuisson, P., Desmons, M., Ferlay, N., and Parol, F.: Cloud information content analysis of multi-angular measurements in the oxygen A-band: application to 3MI and MSPI, *Atmos. Meas. Tech. Discuss.*, 8, 12709-12758, doi:10.5194/amtd-8-12709-2015, 2015.
- [18] Moody, E. G., M. D. King, C. B. Schaaf, and S. Platnick, 2008: MODIS-derived spatially complete surface albedo products: Spatial and temporal pixel distribution and zonal averages. *J. Appl. Meteor. Climatol.*, 47, 2879-2894.
- [19] Nakajima and King, 1990 : Determination of the Optical Thickness and Effective Particle Radius of Clouds from Reflected Solar Radiation Measurements. Part I: Theory. *J. Atmos. Sci.*, vol. 47, 1878-1893.
- [20] Parol et al, 1999 : First Results of the POLDER “Earth Radiation Budget and Clouds” Operational Algorithm. *IEEE Trans. Geosci. Remote Sensing*, vol. 37, 1597-1612.
- [21] J. Riedi, B. Marchant, S. Platnick, B. A. Baum, F. Thieuleux, C. Oudard, F. Parol, J.-M. Nicolas, and P. Dubuisson, Cloud thermodynamic phase inferred from merged POLDER and MODIS data, *Atmos. Chem. Phys.*, 10, 11851-11865, doi:10.5194/acp-10-11851-2010, 2010
- [22] Schaaf, C., F. Gao, A. H. Strahler, W. Lucht, X. Li, T. Tsang, N. C. Strugnell, X. Zhang, Y. Jin, and Muller J. P.: First operational BRDF, albedo nadir reflectance products from MODIS, *Remote Sens. Environ.*, 83(1), 135-148, 2002.
- [23] Souichiro Hioki, Ping Yang, Bryan A. Baum, Steven Platnick, Kerry G. Meyer, Michael D. King, and Jerome Riedi, Degree of ice particle surface roughness inferred from polarimetric observations, *Atmos. Chem. Phys.*, 16, 7545-7558, doi:10.5194/acp-16-7545-2016, 2016
- [24] Sourdeval, O., C-Labonnote, L., Brogniez, G., Jourdan, O., Pelon, J., and Garnier, A.: A variational approach for retrieving ice cloud properties from infrared measurements: application in the context of two IIR validation campaigns, *Atmos. Chem. Phys.*, 13, 8229-8244, doi:10.5194/acp-13-8229-2013, 2013.
- [25] Sourdeval, O., C.-Labonnote, L., Baran, A. J. and Brogniez, G. (2015), A methodology for simultaneous retrieval of ice and liquid water cloud properties. Part I: Information content and case study. *Q.J.R. Meteorol. Soc.*, 141: 870–882. doi:10.1002/qj.2405
- [26] Shang, H., Chen, L., Bréon, F. M., Letu, H., Li, S., Wang, Z., and Su, L.: Impact of cloud horizontal inhomogeneity and directional sampling on the retrieval of cloud droplet size by the POLDER instrument, *Atmos. Meas. Tech.*, 8, 4931-4945, doi:10.5194/amt-8-4931-2015, 2015.
- [27] Wind, G., S. Platnick, M. D. King, P. A. Hubanks, M. J. Pavolonis, A. K. Heidinger, P. Yang and B. A. Baum. 2010, «Multilayer cloud detection with the MODIS near-infrared water vapor absorption band», *J. Appl. Meteor. Clim.*, vol. 49, doi :10.1175/2010JAMC2364.1, p. 2315–2333.
- [28] Yang, P., L. Bi, B. A. Baum, K.-N. Liou, G. Kattawar, M. Mishchenko, and B. Cole, 2013: Spectrally consistent scattering, absorption, and polarization properties of atmospheric ice crystals at wavelengths from 0.2  $\mu\text{m}$  to 100  $\mu\text{m}$ . *J. Atmos. Sci.*, 70, 330-347.

- [29] S. Zeng, C. Cornet, F. Parol, J. Riedi, and F. Thieuleux, A better understanding of cloud optical thickness derived from the passive sensors MODIS/AQUA and POLDER/PARASOL in the A-Train constellation, *Atmos. Chem. Phys.*, 12, 11245-11259, doi:10.5194/acp-12-11245-2012, 2012
- [30] Z. Zhang, P. Yang, G. Kattawar, J. Riedi, L. C. -Labonnote, B. A. Baum, S. Platnick, and H.-L. Huang, Influence of ice particle model on satellite ice cloud retrieval: lessons learned from MODIS and POLDER cloud product comparison, *Atmos. Chem. Phys.*, 9, 7115-7129, doi:10.5194/acp-9-7115-2009, 2009

## 10 List of figures

Figure 1: Summary of individual tests implemented for the cloud detection algorithm (Figure courtesy B. Fougnie – Eumetsat) .....	8
Figure 2: Illustration of the decision tree and input criteria used for multilayered clouds detection.....	9
Figure 3: Schematic diagram of the prototype code structure, main functions and logical workflow.....	14
Figure 4: Example of ECMWF profiles for Ice and Liquid Water Content used to introduce ..	18
Figure 5: Comparison between the AVHRR binary (ice/liquid) phase mask used for TDS V3.2 simulation (left) and the ice fraction computed from ECMWF reanalysis when integrating the IWC/LWC vertical profiles down to an optical depth of 1.0 (center) or 5.0 (right).....	19
Figure 6: Comparison of retrieved effective radius with average value obtained when integrating cloud particle size profiles from cloud top down to an optical depth of 1.0 (left), 5.0 (center) and 10 (right). .....	20
Figure 7 : Example of cloud mask detection (top left) against assumed AVHRR Cloud Mask (top right) and classification scores (bottom).....	21
Figure 8 : Example of cloud phase detection (top left) against assumed AVHRR Cloud phase (top right) and classification scores (bottom). .....	22
Figure 9: Example of cloud top pressure retrieved from polarization Rayleigh scattering signal and scene apparent pressure from O2-A band differential absorption. ....	23
Figure 10 : Cloud top pressure retrieved from O2-A band algorithm (CLOVES output – top left) against assumed AVHRR cloud top pressure (top right) along with global comparison scatterplot (bottom left).....	24
Figure 11 : Comparison between O2-A band retrieved and assumed cloud top pressure for different categories of retrieved and assumed cloud phase.....	25
Figure 12: Example of Cloud Apparent Pressure (derived from O2-A band – left), cloud middle pressures (CLOVES algorithm estimate) and standard deviation of the multiangle retrievals of Cloud Apparent Pressure.....	26
Figure 13: Cloud geometrical thickness retrieved from Cloud Top and Cloud Middle Pressure (left) and Cloud Geometrical Thickness inferred from standard deviation of the multiangle O2-A band cloud apparent pressure retrievals. ....	27
Figure 14 : Example of multilayer flag output from the multi-layered cloud detection algorithm. Here for TDS V3.2, the probability of multilayer situation is low everywhere due to single cloud layer assumptions. ....	28
Figure 15: Example of cloud optical thickness retrieved (top left) against assumed cloud optical thickness from AVHRR products (top right). A global scatterplot (left) shows the general good agreement between assumed and retrieved cloud optical thickness as well as outliers caused by erroneous phase detection.....	29
Figure 16 : Scatterplots of assumed against retrieved cloud optical thickness for different combinations of assumed/retrieved cloud top phase. Agreement between retrieved and assumed optical thickness is generally very good when cloud phase can be determined consistently, while erroneous phase assumptions lead to systematic biases in cloud optical thickness retrievals.....	30
Figure 17: Example of cloud particle effective radius retrieved (top left) against assumed cloud particle effective radius from AVHRR products (top right). A global scatterplot (left) shows the general good agreement between assumed and retrieved cloud particle effective radius as well as outliers caused by erroneous phase detection. ....	31

Figure 18 : Comparison between assumed and retrieved cloud particle effective radius for different combination of retrieved/assumed cloud phase. Agreement is generally good when cloud phase detection agrees with assumed optical properties used for test data simulation. ....	32
Figure 19: Example of Cloud Spherical Albedo and integrated Shortwave Albedo products retrieved from Test Data Set V3.0 .....	33
Figure 20 : Example of cloud mask detection (top left) against assumed AVHRR Cloud Mask (top right) and classification scores (bottom). ....	34
Figure 21 : Example of cloud phase detection (top left) against assumed ECMWF Cloud phase (top right) and classification scores (bottom). ....	35
Figure 22: Example of cloud top pressure retrieved from polarization Rayleigh scattering signal and scene apparent pressure from O2-A band differential absorption. ....	36
Figure 23 : Cloud top pressure retrieved from O2-A band algorithm (CLOVES output – top left) against estimated cloud top pressure from ECMWF inputs (top right) along with global comparison scatterplot (bottom left). ....	37
Figure 24 : Comparison between O2-A band retrieved and assumed cloud top pressure for different categories of retrieved and assumed cloud phase.....	38
Figure 25 : Example of Cloud Apparent Pressure (derived from O2-A band – left), cloud middle pressures (CLOVES algorithm estimate) and standard deviation of the multiangle retrievals of Cloud Apparent Pressure.....	39
Figure 26: Cloud geometrical thickness retrieved from Cloud Top and Cloud Middle Pressure (left), Cloud Geometrical Thickness inferred from standard deviation of the multiangle O2-A band cloud apparent pressure retrievals (centre) and Geometrical Thickness assumed for test data simulation from ECMWF.....	40
Figure 27: Comparison between Cloud Geometrical Thickness(CGT) inferred from differences between CTOP and CMOP (left) and CGT derived from multiangle standard deviation of PAPP. ....	40
Figure 28: Example of multilayer flag output from the multi-layered cloud detection algorithm. Here for TDS V4, the probability of multilayer situations exhibit a large range due to the extended and variable ECMWF cloud profiles used for simulation. ....	41
Figure 29 : Example of cloud optical thickness retrieved (top left) against assumed cloud optical thickness from a combination of AVHRR products and ECMWF profiles (top right). A global scatterplot (left) shows the general good agreement between assumed and retrieved cloud optical thickness as well as outliers caused by erroneous phase detection. ....	42
Figure 30 : Scatterplots of assumed against retrieved cloud optical thickness for different combinations of assumed/retrieved cloud top phase. Correlation between retrieved and assumed optical thickness is very good for liquid clouds but erroneous phase assumptions and multilayer situations (ice over liquid detected as ice only) lead to systematic biases in cloud optical thickness retrievals. ....	43
Figure 31: Example of cloud particle effective radius retrieved (top left) against assumed cloud particle effective radius from AVHRR products (top right). A global scatterplot (left) shows the general good agreement between assumed and retrieved cloud particle effective radius as well as outliers caused by erroneous phase detection and/or vertically inhomogeneous layers assumptions (especially for ice clouds). ....	44
Figure 32: Comparison between assumed and retrieved cloud particle effective radius for different combination of retrieved/assumed cloud phase. Agreement is generally good when	

cloud phase detection agrees with assumed optical properties used for test data simulation. ....	45
Figure 33: Example of Cloud Spherical Albedo and integrated Shortwave Albedo products retrieved from Test Data Set V4.0. ....	46
Figure 34: Statistics of detection agreement for the Cloud Phase product aggregated for the 3 available orbits of TDS V4.1 .....	50
Figure 35: Example of retrieval of a cloud extinction and effective radius vertical profile using 3MI channels in an optimal estimation retrieval framework.....	55
Figure 36: Example of validation of Ztop, CGT and COT retrievals obtained from the enhanced cloud vertical extent retrieval algorithm. Retrievals are compared to analog operational products from POLDER, MODIS and/or CLOUDSAT/CALIPSO. ....	56